



**HAL**  
open science

## **Immobilization of Keggin-type polyoxometalates in cyclodextrin-based polymers for oxidation catalysis**

Sana Aniba, Nathalie Leclerc, Clément Falaise, Catherine Roch-Marchal, Samah Akriche, Emmanuel Cadot, Mohamed Haouas

### ► **To cite this version:**

Sana Aniba, Nathalie Leclerc, Clément Falaise, Catherine Roch-Marchal, Samah Akriche, et al.. Immobilization of Keggin-type polyoxometalates in cyclodextrin-based polymers for oxidation catalysis. Dalton Transactions, 2025, 54 (33), pp.12534-12549. <10.1039/d5dt01317h>. <hal-05215490>

**HAL Id: hal-05215490**

**<https://hal.science/hal-05215490v1>**

Submitted on 20 Aug 2025

**HAL** is a multi-disciplinary open access archive for the deposit and dissemination of scientific research documents, whether they are published or not. The documents may come from teaching and research institutions in France or abroad, or from public or private research centers.

L'archive ouverte pluridisciplinaire **HAL**, est destinée au dépôt et à la diffusion de documents scientifiques de niveau recherche, publiés ou non, émanant des établissements d'enseignement et de recherche français ou étrangers, des laboratoires publics ou privés.



HAL Authorization

# Immobilization of Keggin-type polyoxometalates in cyclodextrin-based polymers for oxidation catalysis

Sana Aniba,<sup>a, b</sup> Nathalie Leclerc,<sup>b</sup> Clément Falaise,<sup>b</sup> Catherine Roch-Marchal,<sup>b</sup> Samah Akriche,<sup>a</sup> Emmanuel Cadot,<sup>b</sup> Mohamed Haouas<sup>\*b</sup>

<sup>a</sup> Laboratory of Chemical Materials, Faculty of Sciences of Bizerte, Carthage University, 7021, Zarzouna, Tunisia

<sup>b</sup> Institut Lavoisier de Versailles, UMR 8180 CNRS, UVSQ, Université Paris-Saclay, Versailles, France

**ABSTRACT:** Immobilization of polyoxometalates (POMs) in organic materials by electrostatic attraction has emerged as one of the most effective methods to design robust and efficient heterogeneous catalysts. However, alternative strategies based on other weak supramolecular interactions, such as molecular recognition, remain less explored. In the present work, we investigate the adsorption capacity of insoluble  $\gamma$ -cyclodextrin ( $\gamma$ -CD) based polymers towards Keggin-type POMs driven by the chaotropic effect, to design supramolecular hybrid composites for oxidative catalysis. First, the polymeric host materials were synthesized by crosslinking  $\gamma$ -CD with epichlorohydrin (EPI) and fully characterized by infrared spectroscopy, solid state NMR and thermal gravimetric analysis (TGA). Four POMs,  $[\text{PW}_{12}\text{O}_{40}]^{3-}$ ,  $[\text{PV}^{\text{V}}\text{W}_{11}\text{O}_{40}]^{4-}$ ,  $[\text{PV}^{\text{IV}}\text{W}_{11}\text{O}_{40}]^{5-}$ , and  $[\text{H}_2\text{W}_{12}\text{O}_{40}]^{6-}$ , with different ionic charges and chemical compositions, were studied to evaluate and compare their adsorption kinetics and equilibrium isotherms. The results show a fast and efficient adsorption process for all POMs, characterized by a pseudo-second order kinetics and a Langmuir isotherm model. The obtained POM@CD-EPI hybrids were then tested as heterogeneous catalysts in the oxidation reaction of benzyl alcohol. Excellent catalytic performances in terms of conversion (up to 100%), selectivity towards benzoic acid (up to 100%), and recyclability (up to 5 cycles) was achieved under mild conditions (60°C/24 h) using tertbutyl hydroperoxide as oxidizing agent. However, the use of  $\text{H}_2\text{O}_2$  as an oxidant led to lower catalytic performance due to the rapid degradation of the POM-polymer composites under these conditions. It is then proposed that the POM-CD host-guest supramolecular arrangement plays a key role in both catalyst stability and the selective oxidation mechanism.

## Introduction

Polyoxometalates (POMs) represent a class of water-soluble ionocovalent oxides built from group V and VI transition metals of high oxidation states such as  $V^{IV/V}$ ,  $Mo^{V/VI}$  or  $W^{V/VI}$ .<sup>1</sup> Vanadium-containing mixed POMs are attracting attention because of their outstanding performance in homogeneous and heterogeneous oxidation catalysis for the conversion of organic substrates.<sup>2–5</sup> Keggin or Dawson-type vanadotungstate structures are generally obtained from an aqueous solution by selective addition of vanadium centers onto vacant POMs containing tetrahedron heteroatoms, such as  $P^V$ . Association of POMs with organic units has attracted growing interest in recent years for the added value these hybrids provide, notably synergistic effects between organic and inorganic moieties in catalysis applications.<sup>6–10</sup>

Heterogeneous catalysis with POMs is preferred for practical reasons, in particular to facilitate catalyst recycling.<sup>11</sup> In the past few decades, many supports have been examined for the immobilization of POMs, e.g., silica, ion-exchange resins, polymers, ionic-liquids, and metal-organic frameworks (MOFs).<sup>12–16</sup> Encapsulation of POMs in various polymer materials, such as microgels, ionogels or biopolymers, can be achieved through various physicochemical processes to obtain responsive multifunctional materials with improved optical, mechanical or magnetic properties.<sup>17–19</sup> Incorporation of POM anions in these hosting matrices usually occurs via weak supramolecular interactions, such as hydrogen bonds, electrostatic attraction, and ion dipole supported by solvent effects.

POMs, particularly those with lower charge density, can form very stable host-guest complexes with organic macrocycles such as  $\gamma$ -cyclodextrin ( $\gamma$ -CD) via molecular recognition processes.<sup>20,21</sup> Their supramolecular association with  $\gamma$ -CD dramatically improves their hydrolytic stability and significantly alters their properties such as solubility, redox behavior, or reactivity.<sup>22–24</sup> In particular, improved catalytic performances are expected from these hybrids in terms of structural robustness against severe reactions conditions, such as temperature, pH, or corrosive environment.<sup>25</sup> Native CDs have shown a remarkable ability to form MOF-type ordered extended networks with POMs exhibiting an enhanced capacity for capturing ionic species, e.g., lithium cations or polyiodides.<sup>26,27</sup> CDs can also form polymeric structures when combined with

crosslinking agents owing to their numerous –OH groups. Such condensation processes lead to stable bonds with different crosslinking units, often resulting in polymers of varying water solubility and molecular weight.<sup>28</sup> Among the most readily available CD crosslinkers are diisocyanates, active carbonyl compounds, and epichlorohydrin (EPI).<sup>29</sup> Immobilization of POMs in CD-based polymers has only recently been achieved with  $\alpha$ - and  $\beta$ -type CDs using hexamethyl diisocyanate (HDI)<sup>21,30</sup> and diphenyl carbonate,<sup>31</sup> respectively. In these hybrids and other similar POM-containing biopolymers, the host-guest interaction often results from the interplay of several phenomena such as inclusion, hydrogen bonding, and the chaotropic effect as driving forces for the self-assembly process.<sup>32–34</sup>

Herein, this study aims to prepare guest-host POM-CD composites as heterogeneous catalysts for the oxidative reaction of organic substrates. EPI-crosslinked  $\gamma$ -CD polymers were first synthesized to serve as extended host matrices for the capture and immobilization of archetypal Keggin-type POMs (**Fig. 1**). Polymerization of this large macrocyclic CD to obtain water-insoluble materials in high yield was found less efficient with the HDI crosslinker than the EPI crosslinker. Detailed adsorption kinetics and isotherms were then carried out to optimize composite synthesis. Finally, the catalytic performances of the resulting hybrid materials were evaluated in the benzyl alcohol (BnOH) oxidation reaction.

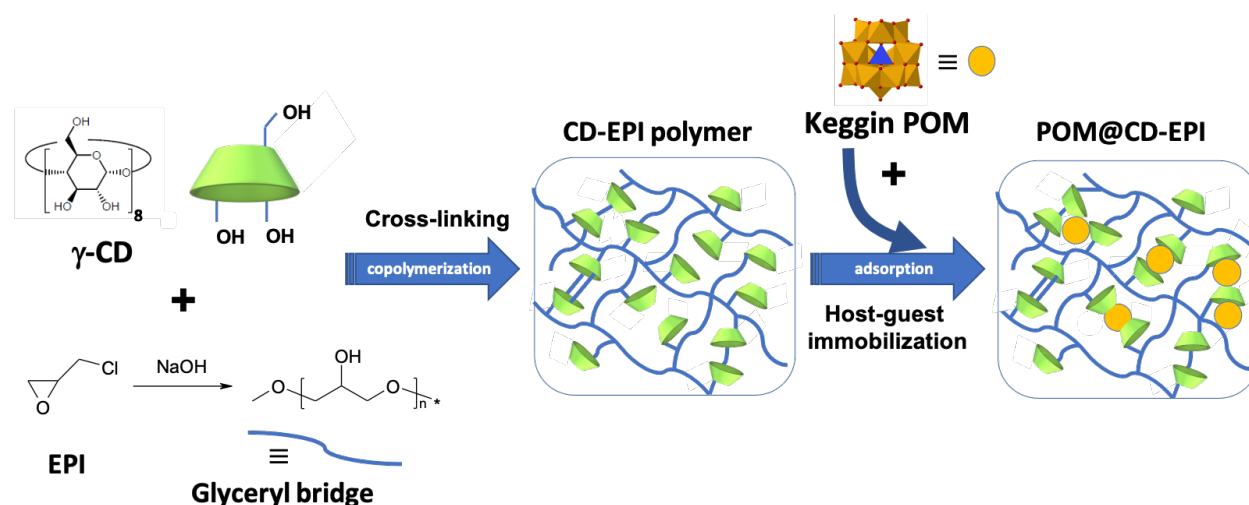


**Fig. 1.** Schematic representation of the immobilization of Keggin POM in a polymeric network of  $\gamma$ -CD copolymerized with epichlorohydrin.

## Results and Discussion

### CD-EPI Polymer synthesis and characterization

Polymer synthesis procedure is described in the ESI<sup>†</sup>. Three CD-EPI(X) polymers were prepared by varying the molar ratio  $X = \text{EPI/CD}$ . The solid products CD-EPI(15) and CD-EPI(20) obtained with 15 and 20 equivalents of EPI were found to be water-soluble, while synthesis with a larger amount of EPI (25 equivalents) gave a CD-EPI(25) polymer that was insoluble in water. This is consistent with the general trend that insoluble polymers are favored for higher EPI/CD, although many other synthesis parameters can also be taken into account, such as temperature, reaction time and base strength.<sup>35,36</sup> The nature of the CD must also be considered, as their reactivity differs significantly depending on the size of the macrocycle. Most studies reported in the literature have focused on the use of  $\beta$ -CD, and very little data are available on EPI-based polymers coupled to  $\gamma$ -CD.

NMR spectroscopy is a technique of choice for characterizing CD-EPI polymers, as it can quantify the degree of co-condensation between the CD and EPI moieties, and hence the CD content.<sup>37,38</sup> For soluble polymers, solution  $^1\text{H}$  NMR is preferred, while  $^{13}\text{C}$  MAS NMR is more useful for solid samples. The  $^1\text{H}$  NMR spectra of the two soluble polymers, CD-EPI(15) and CD-EPI(20), are compared to the spectrum of the native  $\gamma$ -CD in **Fig. S1**, in the Electronic Supplementary Information (ESI<sup>†</sup>). Native  $\gamma$ -CD exhibits six magnetically different types of protons, denoted  $\text{H}_i$ , where  $i = 1$  to 6 (see **Fig. 2**), whereas soluble polymers are characterized by much broader signals and poorly resolved spectra. These broadenings result from a wider distribution of local chemical environments in long chain molecules, but also from a significant decrease in the rotational correlation times due to larger, slower-moving molecules. Because of the lack of resolution, the signals from the polyglycerol chains representing the 'EPI' moieties could not be observed and are superimposed on the  $\text{H}_2$ - $\text{H}_6$  signals from the CD. However, their presence can be easily detected by integrating the signals in the range 3.2-4.2 ppm against the  $\text{H}_1$  signal, which is not involved in any overlap (see ESI<sup>†</sup> for details).  $^{13}\text{C}\{^1\text{H}\}$  NMR spectra of the soluble and insoluble polymers are shown in **Fig. 2**. The solution  $^{13}\text{C}\{^1\text{H}\}$  NMR spectrum of the soluble polymer reveals that each carbon atom in the six-atom unit has a distinct electronic

environment, but undergoes some line broadening due to its inclusion within polymeric matrix. We also note new features near signals C2 and C3 that could indicate that most of the condensation has occurred on the secondary rim of the macrocycle. Signals at ca. 62.5 ppm are observed and attributed to the glycerol functions due to EPI condensation. In the solid-state spectra, all resonances are broadened and partially or totally overlapped as those of polyglycerol moieties. The C1 carbon in the anomeric position is characterized by a deshielded signal at ca. 103 ppm, and is therefore sufficiently resolved to be used to quantify the mass fraction of CD in the polymer (see Fig. S2, in the ESI† for details).

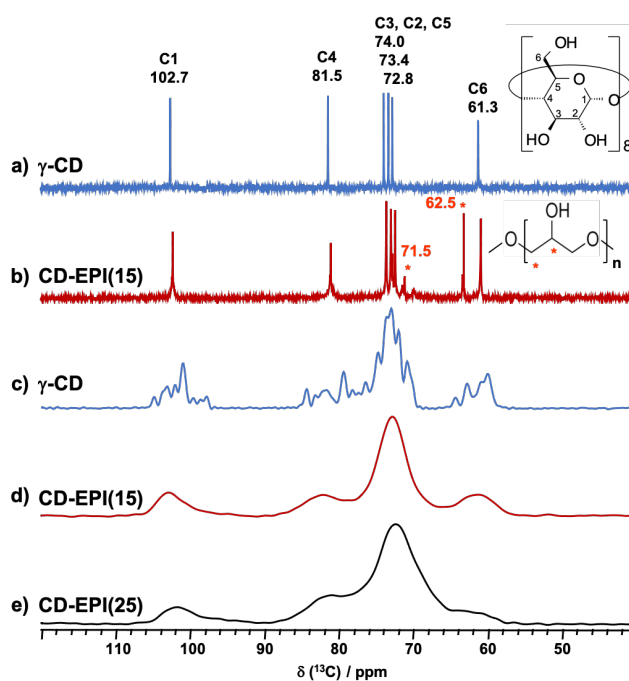


**Fig. 2.**  $^{13}\text{C}\{^1\text{H}\}$  NMR spectra in (a and b)  $\text{D}_2\text{O}$  solution and at (c-e) solid-state of the starting native  $\gamma$ -CD, the soluble CD-EPI(15), and the insoluble polymer CD-EPI(25).

The chemical composition of the polymers can therefore be deduced from these quantitative NMR data, and the results are summarized in Table 1. The EPI/CD molar ratio in the polymer is always lower than the nominal amounts used in the synthesis, meaning that only a fraction of EPI per CD has reacted. The amount of CD in polymer materials remains relatively high, ranging from 50 to 80 wt%, which indicates that these materials are CD-rich. Increasing the

amount of EPI in the synthesis medium produced an insoluble polymer, consistent with previous results,<sup>36</sup> probably favoring cross-linking with CD rather than self-polymerization into polyglycerol chains. Synthesis with a high amount of EPI should then favor multiple crosslinking with a single CD molecule. This may explain why the EPI/CD in the polymer is also steadily increasing linearly. These simultaneous reactions of several OH sites on a CD molecule promote rapid condensation and probably denser polymers. The comparison between solid-state <sup>13</sup>C NMR and solution-state <sup>1</sup>H NMR results on soluble polymers is remarkably consistent, validating the quantification methods, particularly by solid-state NMR for insoluble polymers.

**Table 1:** Polymer composition from quantitative NMR in solution and solid-state.

method	<sup>13</sup> C MAS		<sup>1</sup> H in D <sub>2</sub> O	
	EPI/CD	CD Wt%	EPI/CD	CD Wt%
CD-EPI(15) <sup>a</sup>	7 ± 2	76 ± 4	6 ± 1	80 ± 8
CD-EPI(20) <sup>a</sup>	15 ± 2	60 ± 4	19 ± 2	55 ± 6
CD-EPI(25) <sup>b</sup>	21 ± 7	53 ± 9	-	-

a) Water-soluble polymer; b) insoluble polymer.

Fourier Transform Infrared Spectroscopy (FTIR) is also a valuable tool to provide information on the functional groups present in the polymers.<sup>39</sup> In the IR spectra of the insoluble polymer and  $\gamma$ -CD (see **Fig. S3†**), common bands were observed such as the stretching vibrations of O-H, C-H, and C-C or C-O bonds at 3282, 2923, and 1073 cm<sup>-1</sup>, respectively. Other bands can be observed at 1654 and 1429 cm<sup>-1</sup>, corresponding to the bending deformation of H-O-H and C-O-H bonds, respectively. The absorption band at 2872 cm<sup>-1</sup> is present in the spectrum of CD-EPI polymer but absent in the spectrum of native CD, assigned to the CH/CH<sub>2</sub> group from the glycerol units.

The thermal stability of the insoluble polymer was studied by thermogravimetric analysis (TGA). A careful examination of the thermogravimetric curve, shown in **Fig. S4†**, reveals that intensive washing of the polymer with an acidic buffer solution (see the experimental section in

the ESI<sup>+</sup>) removed almost all the sodium trapped in the polymer during its synthesis ( $\text{R-ONa} + \text{H}^+ \rightarrow \text{R-OH} + \text{Na}^+$ ). The washed insoluble polymer is stable up to 230 °C. Above this temperature, the sample begins to decompose in two stages of mass loss in the temperature range from 230 to 470 °C. The first loss, observed at 100 °C, corresponds to the release of water molecules (8%  $\text{H}_2\text{O}$ ). The final thermal stage, in the temperature range from 230 to 470 °C, is attributed to the progressive degradation of the cyclodextrin-based polymeric structure.

### Adsorption of POMs on CD-EPI polymer

Due to their multiple hydroxyl groups and ether linkages, water-insoluble CD-EPI composites swell when immersed, behaving like a hydrogel. This swelling could lead to the adsorption of POMs according to a process governed by the chaotropic effect taking place in solution where a large part of the polymer would be solvated. To verify this hypothesis, the ability of the synthesized insoluble polymer to adsorb POMs was tested and the optimum adsorption conditions for POM@CD-EPI composites were evaluated. All adsorption experiments, including adsorption kinetics and isotherms, were carried out at room temperature ( $25 \pm 1$  °C), using 75 mg polymer in 5 mL POM solution at pH 1.0, under 500 rpm controlled stirring. Adsorption processes were monitored by UV-Vis spectroscopy for the colored POMs,  $[\text{PV}^{\text{V}}\text{W}_{11}\text{O}_{40}]^{5-}$  and  $[\text{PV}^{\text{V}}\text{W}_{11}\text{O}_{40}]^{4-}$ , and by TGA for colorless POMs  $[\text{PW}_{12}\text{O}_{40}]^{3-}$  and  $[\text{H}_2\text{W}_{12}\text{O}_{40}]^{6-}$ .

Vanadium substituted POM is yellow in its oxidized form  $[\text{PV}^{\text{V}}\text{W}_{11}\text{O}_{40}]^{4-}$ , and turns dark purple when reduced to one electron,  $[\text{PV}^{\text{IV}}\text{W}_{11}\text{O}_{40}]^{5-}$ . Initially, the CD-EPI parent polymer appears as a white powder, and takes on the color of the POM upon adsorption providing a qualitative indication of the efficiency of the adsorption process (**Fig. S5<sup>†</sup>**). The residual concentration of POM in solution was monitored by UV-Vis spectroscopy (**Fig. S6<sup>†</sup>**), following characteristic absorptions of the oxovanadium species observed at 424 nm ( $\epsilon = 1680 \text{ L cm}^{-1} \text{ mol}^{-1}$ ) for the oxidized species  $[\text{PV}^{\text{V}}\text{W}_{11}\text{O}_{40}]^{4-}$ , and at 510 nm ( $\epsilon = 600 \text{ L cm}^{-1} \text{ mol}^{-1}$ ) for the reduced derivative  $[\text{PV}^{\text{IV}}\text{W}_{11}\text{O}_{40}]^{5-}$ .<sup>40,41</sup>

**Fig. 3a** and **3b** show the continuous decrease in UV-Vis absorbance of a  $[\text{PV}^{\text{V}}\text{W}_{11}\text{O}_{40}]^{4-}$  and  $[\text{PV}^{\text{IV}}\text{W}_{11}\text{O}_{40}]^{5-}$  solution as a function of contact time with the CD-EPI(25) polymer. The decrease

in POM concentration in the solution reflects the adsorption process. **Fig. 3c** and **3d** show the evolution of the adsorbed quantity  $q_t$  ( $\mu\text{mol}$  of POM per g of CD polymer) for the two POMs at different initial concentrations ranging from 0.05 to 3.2 mM (see section 1.3 in the ESI† for experimental details). It can be seen that increasing the concentration of POMs continuously increases the maximum equilibrium adsorption quantities  $q_e$  for each concentration. This means that the adsorption capacity of the CD-EPI polymer towards these POMs is far reaching its maximum limit compared to our experimental adsorption conditions (room temperature, pH 1). Furthermore, we find that for low concentrations, adsorption is very fast, reaching equilibrium after only 10 min, and that for high concentrations the equilibrium time increases, but only slightly. Again, this is a strong indication of the high capacity of the CD-EPI(25) polymer to adsorb these POMs. Nevertheless, overall, we observe a slightly higher adsorption capacity for  $[\text{PV}^{\text{V}}\text{W}_{11}\text{O}_{40}]^{4-}$  than for  $[\text{PV}^{\text{IV}}\text{W}_{11}\text{O}_{40}]^{5-}$  at a given concentration.

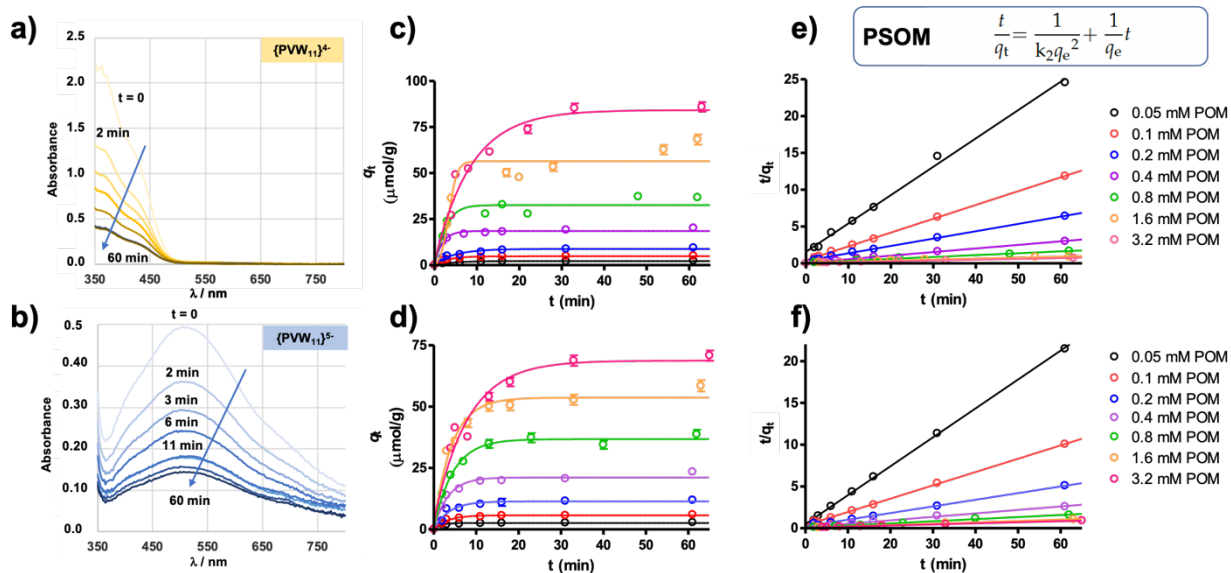


**Fig. 3:** a-b) Evolution of adsorption spectra of  $[\text{PV}^{\text{V}}\text{W}_{11}\text{O}_{40}]^{4-}$  and  $[\text{PV}^{\text{IV}}\text{W}_{11}\text{O}_{40}]^{5-}$  solution (0.8 mM) as a function of contact time with the insoluble polymer CD-EPI(25). c-d) Plots of adsorbed quantity  $q_t$  ( $\mu\text{mol/g}$ ) of  $[\text{PV}^{\text{V}}\text{W}_{11}\text{O}_{40}]^{4-}$  and  $[\text{PV}^{\text{IV}}\text{W}_{11}\text{O}_{40}]^{5-}$  as a function of contact time  $t$  for different POM concentrations, and e-f) its corresponding pseudo-second order model (PSOM) kinetic curves. Experimental conditions: CD polymer amount = 75 mg, POM volume = 5 mL, POM concentration = 0.05-3.2 mM, contact time = 0-60 min, stirring speed = 500 rpm, pH = 1, temperature = 25 °C.

The adsorption kinetic was evaluated considering various kinetic models, i.e., the pseudo-first order model (PFOM), the pseudo-second order model (PSOM), and the interparticle diffusion model (IDM). The best fits of experimental data were obtained with the PSOM presented in **Fig. 3e-f** when compared to the other two models shown in **Fig. S7** and **S8**, in the ESI†. The plot of  $t/q_t$  versus time  $t$  showed almost perfect straight lines over the entire measurement range, and the main parameters of the calculated curves are reported in **Table 2**. The two POMs,  $[\text{PV}^{\text{V}}\text{W}_{11}\text{O}_{40}]^{4-}$  and  $[\text{PV}^{\text{IV}}\text{W}_{11}\text{O}_{40}]^{5-}$ , behave similarly indicating no apparent major effect of the oxidation state of the V center on the adsorption process.

**Table 2:** PSOM kinetic parameters of adsorption of  $\text{PV}^{\text{V}}\text{W}_{11}\text{O}_{40}^{4-}$  and  $\text{PV}^{\text{IV}}\text{W}_{11}\text{VO}_{40}^{5-}$  on CD-EPI(25) polymer.

$C_0$ (mM)	$K_2$ ( $\text{g}\cdot\mu\text{mol}^{-1}\text{min}^{-1}$ )	$q_e$ calc ( $\mu\text{mol}\cdot\text{g}^{-1}$ )	$q_e$ exp ( $\mu\text{mol}\cdot\text{g}^{-1}$ ) <sup>a</sup>	$R^2$
<b><math>\text{PV}^{\text{V}}\text{W}_{11}\text{VO}_{40}^{4-}</math></b>				
0.0457	$0.10 \pm 0.02$	$2.56 \pm 0.07$	2.5	0.9957
0.0984	$0.084 \pm 0.007$	$5.32 \pm 0.03$	5.1	0.9998
0.176	$0.028 \pm 0.004$	$10.0 \pm 0.1$	9.5	0.9991
0.356	$0.030 \pm 0.004$	$20.6 \pm 0.2$	20.2	0.9995
0.713	$0.007 \pm 0.003$	$38 \pm 1$	39	0.9895
1.43	$0.0019 \pm 0.0006$	$73 \pm 4$	68	0.9870
2.84	$0.0015 \pm 0.0003$	$97 \pm 4$	86	0.9913
<b><math>\text{PV}^{\text{IV}}\text{W}_{11}\text{VO}_{40}^{5-}</math></b>				
0.0500	$0.240 \pm 0.04$	$2.89 \pm 0.03$	2.8	0.9996
0.104	$0.07 \pm 0.01$	$6.29 \pm 0.08$	6.06	0.9991
0.205	$0.029 \pm 0.008$	$12.5 \pm 0.3$	11.9	0.9971
0.435	$0.013 \pm 0.004$	$24 \pm 1$	23	0.9973
0.819	$0.008 \pm 0.002$	$40 \pm 1$	39	0.9948
1.69	$0.0049 \pm 0.0009$	$61 \pm 1$	58	0.9984
3.19	$0.0024 \pm 0.0005$	$78 \pm 2$	71	0.9958

a) Value of the last point in the kinetic experiment (i.e., contact time 60 min).

The rapid decrease in adsorption rates with increasing POM concentration can be attributed to a drop in the number of available vacant sites due to the high affinity between POM and the CD-EPI polymer. Indeed, the pseudo second order kinetics observed seem to indicate adsorption dominated by chemical factors.<sup>41</sup> POM molecules present in the adsorption medium can interact more readily with the interaction sites at lower concentrations, resulting in a higher rate constant. On the other hand, at higher concentrations, as saturation approaches, the rate constants of POM adsorption to the polymer drop due to increased competition for the remaining adsorption sites. These observations confirm that chemical forces, e.g., chemisorption, are the main causes of POM adsorption here, as opposed to physical forces, e.g., diffusion.<sup>42,43</sup> Adsorption therefore takes place on specific active sites, probably the central cavity of CD moiety to form inclusion complexes through hydrogen bonds or other driving forces related to the solvent effect. These results are consistent with the assertion that the rate constant of the pseudo-second-order model is a complex function of the initial solute concentration.<sup>31</sup>

Comparison between the results of the two POMs shows comparable orders of magnitude in adsorption rates, although adsorption is slightly faster with  $[PV^VW_{11}O_{40}]^{5-}$  than with  $[PV^VW_{11}O_{40}]^{4-}$  at high concentrations. However, the equilibrium adsorption quantity  $q_e$  was found to be slightly higher with  $[PV^VW_{11}O_{40}]^{4-}$  than with  $[PV^VW_{11}O_{40}]^{5-}$  at high concentrations (see **Table 2**). This observation is consistent with the fact that a high POM loading decreases the adsorption rate, as previously observed. Also, the overall trend showed a slightly better adsorption performance with the less charged POM, as might be anticipated from the chaotropic effect.<sup>19</sup>

To evaluate the POM release capacity of the POM@CD-EPI composites, the samples obtained with 1.6 mM POM were treated in a pH 1 sulfate buffer solution under 500 rpm stirring for 1 h at 25 and 60 °C. UV-Vis (**Fig. S9†**) measurements of supernatants revealed a POM loading loss of only 1.5% and 8% for  $[PV^VW_{11}O_{40}]^{4-}$ , and 7% and 29% for  $[PV^VW_{11}O_{40}]^{5-}$  at RT and 60 °C, respectively. However, in the case of  $[PV^VW_{11}O_{40}]^{4-}$ , we noticed the reduction of POM after its release at 60 °C, with the appearance of the absorption band at 510 nm. This is probably due to the oxidation of few OH groups on the CDs by the POM. These results, confirm that the adsorption is very strong, mainly chemisorption, and that physisorbed POMs, if any, are negligible.

Two other Keggin POMs,  $[\text{PW}_{12}\text{O}_{40}]^{3-}$  and  $[\text{H}_2\text{W}_{12}\text{O}_{40}]^{6-}$ , carrying different negative charges were also studied for comparison. Adsorption equilibrium is reached when the quantity of POM adsorbed no longer changes over time. At this point, the amount of adsorbed POM inside the polymer is in a dynamic equilibrium with the amount of POM desorbed. This equilibrium is reached after 1 h of contact, as previously observed with the other POMs. The adsorption is quantitatively evaluated by TGA, and Fig. 4 presents the results obtained. We note the difference in the thermal decomposition behavior, while with  $[\text{PW}_{12}\text{O}_{40}]@\text{CD-POM}$  the weight loss takes place in three stages and up to 650 °C, with  $[\text{H}_2\text{W}_{12}\text{O}_{40}]@\text{CD-EPI}$  the process is complete at a lower temperature (500 °C) involving only two steps. This may reflect a difference in the thermal stability of the POMs, which is higher for  $[\text{PW}_{12}\text{O}_{40}]^{3-}$  than for  $[\text{H}_2\text{W}_{12}\text{O}_{40}]^{6-}$ . The solid residue obtained at 700 °C corresponds to the elemental oxides which result from the thermal decomposition of the POM, e.g.,  $\text{WO}_3$ ,  $\text{Na}_2\text{O}$ ,  $\text{Rb}_2\text{O}$ , or  $\text{P}_2\text{O}_5$ . Here, we calculate the quantity of POM adsorbed in the solid, we then deduce by subtraction the quantity  $q_e$  resulting from the heterogenous equilibrium between the solid and the solution.

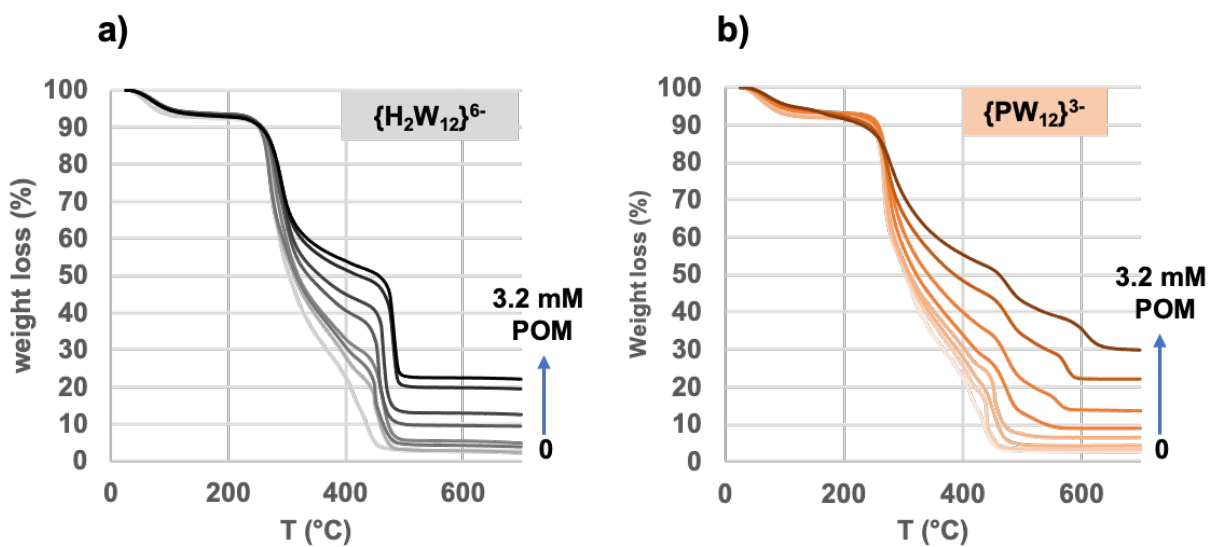


**Fig. 4:** Evolution of TGA curves of POM@CD-EPI composites obtained upon adsorption of 5 mL of a)  $[\text{H}_2\text{W}_{12}\text{O}_{40}]^{6-}$  or b)  $[\text{PW}_{12}\text{O}_{40}]^{3-}$  solutions of varied concentrations on 75 mg of insoluble polymer CD-EPI(25). Experimental conditions: CD polymer amount = 75 mg, POM volume = 5 mL, POM concentration = 0-3.2 mM, contact time = 60 min, stirring speed = 500 rpm, pH = 1, temperature = 25 °C.

To better understand the adsorption equilibrium, the adsorption isotherms are analyzed with the Langmuir model (see 1.3 section of the ESI†). The calculated curves are shown in **Fig. 5**. The parameters extracted from fitting of the experimental data are collected in **Table 3**. Extrapolation of the calculated models allowed to estimate maximum adsorption capacity  $q_{\max}$ . The highest value of  $135 \mu\text{mol}\cdot\text{g}^{-1}$  was found for  $[\text{PW}_{12}\text{O}_{40}]^{3-}$ , well above the values obtained for  $[\text{PV}^{\text{V}}\text{W}_{11}\text{O}_{40}]^{5-}$  and  $[\text{H}_2\text{W}_{12}\text{O}_{40}]^{6-}$  in the  $75\text{-}90 \mu\text{mol}\cdot\text{g}^{-1}$  range. This observation is in line with the general trend that follows the negative charge of POM, i.e., the lower the charge, the higher the adsorption capacity. The affinity for complexation at the molecular level between the  $\gamma$ -CD and Keggin-type POMs in aqueous solution is known to be mainly governed by the chaotropic character of the POM which directly depends on the charge density of the nanoion.<sup>17,20</sup> These values also indicate that the POM/CD molar ratio decreases from 0.33, to 0.25, to ca. 0.2 when decreasing the charge from 3-, to 4-, to -5/6, clearly showing that only small fraction of CD are accessible to POM. Both thermodynamic and  $R_L$  values indicate a favorable and spontaneous adsorption process. The  $R_L$  parameter varying from 0 to 1 across the studied POM concentration range, 0.05-3.2 mM, is consistent with favorable adsorption.<sup>39,44</sup> Consequently, the  $\Delta G$  associated with adsorption process is negative, and falls in all cases in common values between  $-27$  and  $-26 \text{ kJ}\cdot\text{mol}^{-1}$ . These results demonstrate comparable strong affinity of the CD-EPI polymer towards Keggin POMs.

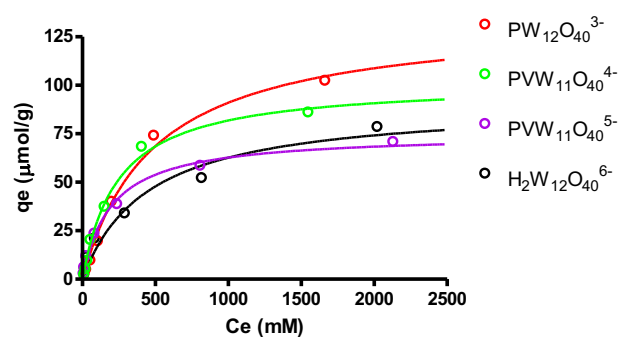


**Fig. 5:** Langmuir isotherm curves for adsorption of  $[\text{PW}_{12}\text{O}_{40}]^{3-}$ ,  $[\text{PV}^{\text{V}}\text{W}_{11}\text{O}_{40}]^{4-}$ ,  $[\text{PV}^{\text{V}}\text{W}_{11}\text{O}_{40}]^{5-}$ , and  $[\text{H}_2\text{W}_{12}\text{O}_{40}]^{6-}$  on insoluble polymer CD-EPI(25). Experimental conditions: CD polymer amount = 75 mg, POM volume = 5 mL, POM concentration = 0-3.2 mM, contact time = 60 min, stirring speed = 500 rpm, pH = 1, temperature = 25 °C.

**Table 3:** Adsorption isotherm parameters from fitting curves of Fig. 5<sup>a</sup> with Langmuir model
$$(q_e = \frac{\frac{K_L}{a_L} C_e}{\frac{1}{a_L} + C_e}),$$
 and deduced maximum POM<sub>max</sub>/CD capacity in CD-EPI(25) composite

POM	$K_L$ (L.g <sup>-1</sup> )	$q_{max}$ (μmol.g <sup>-1</sup> ) <sup>b</sup>	$a_L$ (L.μmol <sup>-1</sup> )	$\Delta G^\circ$ (kJ.mol <sup>-1</sup> ) <sup>c</sup>	$R_L$ <sup>d</sup>	POM <sub>max</sub> per CD <sup>e</sup>
[PW <sub>12</sub> O <sub>40</sub> ] <sup>3-</sup>	0.28 ± 0.03	135 ± 9	0.0020 ± 0.0003	-26.5 ± 0.2	0.113 - 0.907	0.33
[PV <sup>V</sup> W <sub>11</sub> O <sub>40</sub> ] <sup>4-</sup>	0.43 ± 0.04	102 ± 4	0.0042 ± 0.0005	-27.4 ± 0.2	0.078 - 0.840	0.25
[PV <sup>IV</sup> W <sub>11</sub> O <sub>40</sub> ] <sup>5-</sup>	0.38 ± 0.04	75 ± 3	0.0050 ± 0.0008	-27.1 ± 0.3	0.059 - 0.800	0.18
[H <sub>2</sub> W <sub>12</sub> O <sub>40</sub> ] <sup>6-</sup>	0.23 ± 0.03	90 ± 10	0.0025 ± 0.0006	-26.0 ± 0.3	0.111 - 0.889	0.22

a) Determination coefficient  $R^2$  in the range of 0.97-0.99. b)  $q_{max} = K_L/a_L$ ; c)  $\Delta G^\circ = -RT \ln(MW_{POM}C_{H_2O}K_L)$ .  
d)  $R_L = 1/(1+a_L C_0)$  for POM concentration range  $C_0$  0.05-3.2 mM. e) Calculated from  $q_{max}$  and 53 wt% CD.

### Characterization of POM@CD-EPI composites

The final composites obtained by adsorption of a 3.2 mM POM solution onto the insoluble CD-EPI(25) polymer were subjected to further characterization by various techniques, including TGA, elemental analysis, FT-IR, and solid-state NMR spectroscopy. The main objective of these analyzes is to identify and verify the chemical structure and composition of the POM and its interaction with its local environment.

The TGA of [PVW<sub>11</sub>O<sub>40</sub>]<sup>4-/5-</sup>@CD-EPI composites (**Fig. S10<sup>†</sup>** and **S11<sup>†</sup>**) showed final plateau with a difference of 17 and 21 wt% with respect to the plateau of the parent polymer, corresponding to POM residues of [PV<sup>IV</sup>W<sub>11</sub>O<sub>40</sub>]<sup>5-</sup> and [PV<sup>V</sup>W<sub>11</sub>O<sub>40</sub>]<sup>4-</sup>, respectively. These amounts correspond to 70 and 91 μmol POM per 1 g of polymer, in perfect agreement with the values obtained by UV-Vis spectroscopy of 71 and 86 μmol.g<sup>-1</sup> observed with [PV<sup>IV</sup>W<sub>11</sub>O<sub>40</sub>]<sup>5-</sup> and [PV<sup>V</sup>W<sub>11</sub>O<sub>40</sub>]<sup>4-</sup>, respectively. Quantitative elemental analyzes were carried out to calculate the amount of POM adsorbed in the polymer (**Tables S1<sup>†</sup>** and **S2<sup>†</sup>**). ICP analyzes tend to underestimate the P and V contents, while EDS measurement overestimates the P content. However, the observed P/V and W/V molar ratio of 1 and 11, respectively, match the expected values for an intact POM structure. The amounts of cation (Na and K) in the composites were

found to be too low (ca. 30  $\mu\text{mol}\cdot\text{g}^{-1}$ ) to compensate for the negative charge of the POM. This content is very similar that initially present in the parent polymer CD-EPI(25), indicating that the adsorbed POMs are rather in their protonic forms, i.e., heteropolyacids. Thus, the chemical formula of the inorganic part in the composites based on ICP analyses is  $\text{Na}_x\text{H}_{n-x}[\text{PVW}_{11}\text{O}_{40}]$ , with  $x = 0.4\text{-}0.5$  and  $n = 4$  or  $5$  (for both reduced and oxidized POMs).

The functional groups of the polymer that are responsible for interactions with the POMs could be determined by FT-IR. **Fig. S3†** shows the FT-IR spectra of the POM@polymer composites compared to that of the POM used  $\text{K}_5[\text{PV}^{\text{IV}}\text{W}_{11}\text{O}_{40}]\cdot 16\text{H}_2\text{O}$ ,  $\text{K}_4[\text{PV}^{\text{V}}\text{W}_{11}\text{O}_{40}]\cdot 9\text{H}_2\text{O}$ , the parent polymer CD-EPI(25), and the native  $\gamma$ -CD. The absorption band at  $2870\text{ cm}^{-1}$ , corresponding to the vibrations of the new carbon skeleton linked to the cyclodextrin rings after copolymerization with the epichlorohydrin,<sup>39</sup> is present in all composite materials. Characteristic POM bands at  $960$  and  $880\text{ cm}^{-1}$ , attributed to  $\text{W}=\text{O}$  stretching and vibrational frequency of  $\text{W}-\text{O}_b-\text{W}$  ( $\text{O}_b$  = corner-sharing O),<sup>45</sup> respectively, are observed in all composite samples. In addition, we observe a slight shift in  $\text{W}-\text{O}_c-\text{W}$  vibrations ( $\text{O}_c$  = edge-sharing O), from  $760$  to  $800\text{ cm}^{-1}$ , which could be attributed to an inclusion effect of POM in the polymer. Similar high-frequency shifts have been observed when POMs are incorporated into mesoporous MOFs.<sup>46,47</sup>

Further analyses were carried out using solid-state NMR, as shown in **Fig. 6**. The  $^{31}\text{P}$  MAS NMR spectra of the POM@CD-EPI composites are compared with the spectra of the corresponding original POM compounds,  $\text{K}_5[\text{PV}^{\text{IV}}\text{W}_{11}\text{O}_{40}]\cdot 16\text{H}_2\text{O}$ ,  $\text{K}_4[\text{PV}^{\text{IV}}\text{W}_{11}\text{O}_{40}]\cdot 9\text{H}_2\text{O}$ , in **Fig. 6a**. The  $^{31}\text{P}$  NMR spectrum of the  $[\text{PV}^{\text{IV}}\text{W}_{11}\text{O}_{40}]^{5-}$  species shows a very broad signal as a result of the paramagnetic nature of the  $\text{V}^{\text{IV}}$  centers, while that of the diamagnetic  $[\text{PV}^{\text{V}}\text{W}_{11}\text{O}_{40}]^{4-}$  contains a very narrow signal due to its highly symmetrical environment in the central cavity of the Keggin structure. The similarity of the spectra of composites with those of their starting POM counterparts, indicates the successful adsorption of POM into the polymer without degradation or redox change of the initial POM.  $^{51}\text{V}$  NMR is only possible for the diamagnetic POM  $[\text{PV}^{\text{V}}\text{W}_{11}\text{O}_{40}]^{4-}$ . The  $^{51}\text{V}$  MAS spectra of  $\text{K}_4[\text{PV}^{\text{V}}\text{W}_{11}\text{O}_{40}]\cdot 9\text{H}_2\text{O}$  and  $[\text{PV}^{\text{V}}\text{W}_{11}\text{O}_{40}]^{4-}$ @CD-EPI shown in **Fig. 6b** are dominated by strong chemical shift anisotropy (CSA), while quadrupolar coupling constants are moderate, of the order of  $1\text{ MHz}$ .<sup>48</sup> Spectra recorded at various MAS rates were simulated using the DMfit program<sup>49</sup> to extract isotropic and anisotropic chemical shift

parameters,  $\delta_{\text{iso}}$ ,  $\Delta_{\text{CSA}}$ , and  $\eta_{\text{CSA}}$  (Fig. S13<sup>†</sup> and S14<sup>†</sup>). For the POM compound  $\text{K}_4[\text{PV}^{\text{V}}\text{W}_{11}\text{O}_{40}]\cdot 9\text{H}_2\text{O}$ , the spectrum shows a composite signal consisting of a main resonance with a small shoulder. The dominant resonance has an isotropic chemical shift  $\delta_{\text{iso}}$  of  $-565.4 \pm 0.3$  ppm, an axial tensor  $\Delta_{\text{CSA}}$  of  $-153 \pm 4$  kHz, an asymmetry parameter  $\eta_{\text{CSA}}$  of  $0.77 \pm 0.06$ , and a full width at half-maximum (fwhm) of 1.0 kHz. The single resonance with its MAS sidebands observed in the composite  $[\text{PV}^{\text{V}}\text{W}_{11}\text{O}_{40}]^{4-}\text{@CD-EPI}$  is characterized by slightly different parameters, i.e.,  $\delta_{\text{iso}} = -553.8 \pm 0.3$  ppm,  $\Delta_{\text{CSA}} = -80 \pm 10$  kHz,  $\eta_{\text{CSA}} = 0.7 \pm 0.1$ , and fwhm = 2.1 kHz. It is particularly interesting to note that the significant line broadening and the lower anisotropy of chemical shift should indicate greater disorder and dispersion at the molecular level of the POM units in the polymer matrix. This comparison clearly shows that there is a wider distribution in the local chemical environment and more structural disorder around the POM in the  $[\text{PV}^{\text{V}}\text{W}_{11}\text{O}_{40}]^{4-}\text{@CD-EPI}$  composite than in the ionic salt  $\text{K}_4[\text{PV}^{\text{V}}\text{W}_{11}\text{O}_{40}]\cdot 9\text{H}_2\text{O}$ .

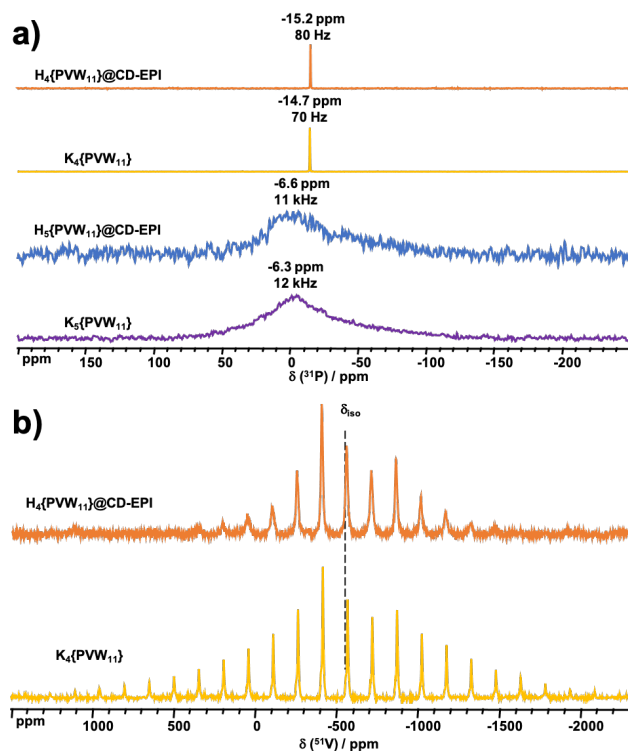


**Fig. 6:** a)  $^{31}\text{P}$  MAS NMR spectra of POM@CD-EPI composites compared with spectra of the original POMs studied  $\text{K}_5[\text{PV}^{\text{V}}\text{W}_{11}\text{O}_{40}]\cdot 16\text{H}_2\text{O}$ , and  $\text{K}_4[\text{PV}^{\text{V}}\text{W}_{11}\text{O}_{40}]\cdot 9\text{H}_2\text{O}$ . b)  $^{51}\text{V}$  MAS NMR spectrum of POM@CD-EPI composite compared with the spectrum of the original POM compound  $\text{K}_4[\text{PV}^{\text{V}}\text{W}_{11}\text{O}_{40}]\cdot 9\text{H}_2\text{O}$ .

## Comparison of POM adsorption performance with literature

Most previous studies on Keggin-type POM adsorption have been carried out on porous catalyst supports such as activated carbon and MOFs,<sup>50–52</sup> while, to our knowledge, no data can be found in the literature on polymeric materials. Wu et al. have studied in detail the adsorption properties of phospho- and silico-molybdate and -tungstate polyacids with the Keggin structure on various activated carbons and other porous materials.<sup>52,53</sup> More recently, MOFs have been shown as potential host materials to encapsulate POMs for a variety of purposes, such as catalysis, energy conversion or environmental remediation.<sup>15,54–60</sup> However, there are very few detailed quantitative adsorption studies on adsorption properties with these types of support, such as adsorption isotherms and kinetics. **Table 4** presents a comprehensive comparison and analysis of available  $q_{\max}$  values for numerous adsorbents and Keggin-type POMs, including our results obtained with the CD-EPI polymer. The most effective adsorbent materials were porous activated carbons and bentonite, with exceptional loading capacity in the range of ca. 400–800  $\mu\text{mol.g}^{-1}$ .<sup>52,61–63</sup> It should be mentioned, however, that this outstanding performance is achieved with phosphomolybdate POM and that tungsten POM counterparts have always shown much lower values (ca. 300  $\mu\text{mol.g}^{-1}$ ).<sup>50</sup> Our results with the CD-EPI polymer range from 75 to 135  $\mu\text{mol.g}^{-1}$ , which is comparable to the adsorption performance of Keggin phosphotungstate on mesoporous MOF compounds showing values between 95 and 165  $\mu\text{mol.g}^{-1}$ .<sup>60,64</sup> However, for the same phosphotungstate POM family, our CD-EPI polymer showed a lower adsorption capacity than activated carbons, i.e., 330  $\mu\text{mol.g}^{-1}$ ,<sup>50</sup> but much higher than that of aluminosilicate bentonite clay (53  $\mu\text{mol.g}^{-1}$ ).<sup>52</sup> These comparisons demonstrate the excellent adsorption performance of our cyclodextrin-based polymer similar to meso- and micro-porous solids such as MOFs or layered oxides. This suggests that the copolymerization of EPI with CD may generate mesoporosity within the polymeric network in conjunction with the preformed ring-shaped CD building blocks that would constitute local cavities for adsorption sites. The influence of POM negative charge on adsorption capacity can also be significant considering the chaotropic effect could contribute to encapsulation process. Indeed, the general tendency shows that adsorption with  $[\text{PM}_{12}\text{O}_{40}]^{3-}$  is always superior to that with  $[\text{SiM}_{12}\text{O}_{40}]^{4-}$ , and the same is true for  $[\text{PVM}_{11}\text{O}_{40}]^{4-}$  compared to  $[\text{PVM}_{11}\text{O}_{40}]^{5-}$  (M = Mo or W).

**Table 4:** Efficiency of different adsorbents towards Keggin-type POMs

<b>POM</b>	<b>Adsorbent</b>	<b><math>q_{\max}</math> (<math>\mu\text{mol.g}^{-1}</math>)</b>	<b>Reference</b>
<b>H<sub>3</sub>[PMo<sub>12</sub>O<sub>40</sub>]</b>	titania	5	65
	silica	11	65
	carbon	11	65
	alumina	15-130	51,65
	bentonite	48	52
	MIL-101(Cr)	285	46
	activated C	355-800	61-63
<b>H<sub>3</sub>[PW<sub>12</sub>O<sub>40</sub>]</b>	bentonite	53	52
	Zr <sub>6</sub> -TCPP-Fe-120	95	64
	MIL-101(Fe)	139	60
	Zr <sub>6</sub> -TCPP-120	165	64
	activated C	330	50
<b>H<sub>4</sub>[SiMo<sub>12</sub>O<sub>40</sub>]</b>	silica	33	66
	bentonite	33	52
	carbon	36	66
	MIL-101(Cr)	279	46
	activated C	285	53
<b>H<sub>4</sub>[SiW<sub>12</sub>O<sub>40</sub>]</b>	diatomite	3	52
	titania	9	52
	bentonite	37	52
	alumina	139	52
	activated C	200	52
<b>H<sub>4</sub>[PV<sup>V</sup>Mo<sub>11</sub>O<sub>40</sub>]</b>	MIL-101(Cr)	259	46
<b>(NH<sub>4</sub>)<sub>5</sub>[PV<sup>IV</sup>Mo<sub>11</sub>O<sub>40</sub>]</b>	MIL-101(Cr)	210	46
<b>Na<sub>3</sub>[PW<sub>12</sub>O<sub>40</sub>]</b>	CD-EPI polymer	135	This work
<b>K<sub>4</sub>[PV<sup>V</sup>W<sub>11</sub>O<sub>40</sub>]</b>	CD-EPI polymer	102	This work
<b>K<sub>5</sub>[PV<sup>IV</sup>W<sub>11</sub>O<sub>40</sub>]</b>	CD-EPI polymer	75	This work
<b>NaRb<sub>5</sub>[H<sub>2</sub>W<sub>12</sub>O<sub>40</sub>]</b>	CD-EPI polymer	90	This work

### Catalytic performance of the POM@CD-EPI composites

The catalytic activity of POM@CD-EPI composites was tested in the oxidation of BnOH to BzOH, using hydrogen peroxide ( $\text{H}_2\text{O}_2$ ) or tert-butyl hydroperoxide (t-BuOOH) as the oxidizing agent (Table 5). The presence of an oxidizing agent in conjunction with a catalyst is necessary to observe a decent conversion (Table 5, entries 16 and 17). Catalysis with POM-only systems (Table 5, entries 8-11) showed comparable conversion in the range 40-50% and selectivity for BzOH around 60%, irrespective of the oxidizing agent or the initial oxidation state of V center ( $\text{V}^{\text{V}}$  or  $\text{V}^{\text{IV}}$ ) in POM. The situation is different for composites, and contrasting results have been obtained depending on the oxidizing agent used and the nature of the POM in the polymer. With  $\text{H}_2\text{O}_2$ , the best performance was achieved with  $\{\text{PW}_{12}\}^{3-}$ @CD-EPI, showing full conversion and selectivity (Table 5, entry 1), but reaction in this medium led to catalyst degradation and POM release. Indeed, the coloration of the collected product (yellow/brown) and the  $^{31}\text{P}$  and  $^{51}\text{V}$  NMR analyses clearly indicate the leaching of POM (see Fig. S15†). In the case of t-BuOOH, the products obtained were always colorless and no catalyst degradation was observed. Surprisingly, the catalytic activity of composites was reversed with this oxidant, i.e.,  $\{\text{PW}_{12}\}^{3-}$ @CD-EPI becomes inactive (Table 5, entry 4), and vanadium-containing POM composites  $\{\text{PVW}_{11}\}^{4/5-}$ @CD-EPI highly efficient (Table 5, entries 5 and 6). These results seem to indicate that oxidation with  $\text{H}_2\text{O}_2$  leads to degradation of the composites, while reaction with t-BuOOH preserves its integrity. Consequently, the system with t-BuOOH is preferred over that with  $\text{H}_2\text{O}_2$ . Moreover, with composites, separation of the catalyst from the products is easy, offering the possibility of recycling, which is not possible in homogeneous POM-only catalysis. We also note the same performance of both POMs regardless their charge (4- or 5-) in the composite, as was observed with POM catalyst alone. This means that the large excess of oxidizing agent continuously regenerates the oxidized POM during the catalytic process, whether starting from the oxidized or reduced form. No special precautions are therefore necessary to protect the catalysts from ambient oxidation. Regarding the effect of cyclodextrin, further experiments were carried with physical mixture of catalyst  $\text{K}_5[\text{PV}^{\text{IV}}\text{W}_{11}\text{O}_{40}]$  and free  $\gamma$ -CD up to 5 eq. (Table 5, entries 12-15). In these cases, the catalysis is no longer homogeneous, as the cyclodextrin was not soluble in these reaction mixtures. Part of the POM remains in the liquid phase as indicated by its color. In the

presence of one eq. of CD relative to POM, excellent performance in terms of conversion and selectivity was observed with t-BuOOH, but not with H<sub>2</sub>O<sub>2</sub>. However, increasing the amount of CD led to a decrease in catalytic performance. Clearly, a large excess of CD inhibits POM activity in these molecular systems, probably due to screening effect. It can be noticed that for POM-polymer even with the CD/POM molar ratio close to 5, the catalytic activity is high, demonstrating the importance of the dispersion of CD inside the polymer.

**Table 5:** Oxidation of BnOH into BzH and BzOH with POM and POM@CD-EPI composites<sup>a</sup>

Entry	Oxidizing agent	Catalyst	Conversion (%) <sup>b</sup>	BzH	BzOH	BzOH
				yield (%) <sup>c</sup>	yield (%) <sup>c</sup>	selectivity (%) <sup>d</sup>
1	H <sub>2</sub> O <sub>2</sub>	{PW <sub>12</sub> } <sup>3-</sup> @CD-EPI <sup>e</sup>	99	1	98	99
2	H <sub>2</sub> O <sub>2</sub>	{PV <sup>V</sup> W <sub>11</sub> } <sup>4-</sup> @CD-EPI <sup>e</sup>	30	9	21	70
3	H <sub>2</sub> O <sub>2</sub>	{PV <sup>IV</sup> W <sub>11</sub> } <sup>5-</sup> @CD-EPI <sup>e</sup>	26	7	19	73
4	t-BuOOH	{PW <sub>12</sub> } <sup>3-</sup> @CD-EPI	4	1	3	75
5	t-BuOOH	{PV <sup>V</sup> W <sub>11</sub> } <sup>4-</sup> @CD-EPI	95	5	90	95
6	t-BuOOH	{PV <sup>IV</sup> W <sub>11</sub> } <sup>5-</sup> @CD-EPI	100	1	99	99
7	t-BuOOH	{H <sub>2</sub> W <sub>12</sub> } <sup>6-</sup> @CD-EPI	58	15	43	74
8	H <sub>2</sub> O <sub>2</sub>	K <sub>4</sub> [PV <sup>V</sup> W <sub>11</sub> O <sub>40</sub> ]	43	17	26	60
9	t-BuOOH	K <sub>4</sub> [PV <sup>V</sup> W <sub>11</sub> O <sub>40</sub> ]	49	18	31	63
10	H <sub>2</sub> O <sub>2</sub>	K <sub>5</sub> [PV <sup>IV</sup> W <sub>11</sub> O <sub>40</sub> ]	46	17	29	63
11	t-BuOOH	K <sub>5</sub> [PV <sup>IV</sup> W <sub>11</sub> O <sub>40</sub> ]	86	9	77	90
12	H <sub>2</sub> O <sub>2</sub>	K <sub>5</sub> [PV <sup>IV</sup> W <sub>11</sub> O <sub>40</sub> ]+ 1 eq. CD	58	9	48	84
13	t-BuOOH	K <sub>5</sub> [PV <sup>IV</sup> W <sub>11</sub> O <sub>40</sub> ]+ 1 eq. CD	99	1	98	99
14	t-BuOOH	K <sub>5</sub> [PV <sup>IV</sup> W <sub>11</sub> O <sub>40</sub> ]+ 2 eq. CD	66	20	46	70
15	t-BuOOH	K <sub>5</sub> [PV <sup>IV</sup> W <sub>11</sub> O <sub>40</sub> ]+ 5 eq. CD	21	13	8	38
16	no oxidant	{PV <sup>IV</sup> W <sub>11</sub> } <sup>5-</sup> @CD-EPI	1	1	0	0
17	t-BuOOH	no catalyst	4	4	0	0

a) Reaction conditions: 2 mmol substrate (BnOH), 12.5 mmol oxidizing agent (H<sub>2</sub>O<sub>2</sub> or t-BuOOH), 0.01 mmol catalyst (POM), 60 °C, 24 h. b) C (%) = (1 - *f*<sub>BnOH</sub>) × 100. c) Y<sub>product</sub> (%) = *f*<sub>product</sub> × 100. d) S<sub>BzOH</sub> (%) = *f*<sub>BzOH</sub> × 100 / (*f*<sub>BzOH</sub> + *f*<sub>BzH</sub>); *f* = molar fraction. e) POM leaching/catalyst degradation.

These initial results show that the best catalytic system is the tandem  $\{PVW_{11}\}^{4/5-}@CD-EPI$  composites and t-BuOOH as catalyst and oxidizing agent, respectively. Therefore, we focused on the  $\{PV^{IV}W_{11}\}^{5-}@CD-EPI$  / t-BuOOH system to study and optimize experimental conditions. **Fig. 7** summarizes the results obtained from investigations into the effects of temperature, solvent, and substrate quantity, as well as kinetics and recyclability studies. Although the catalytic performance obtained at 60 °C / 24 h is quite good, we attempted to reduce the reaction time by increasing the temperature. However, we observed that increasing the reaction temperature is accompanied by catalyst degradation, manifested by POM release and polymer disintegration. **Fig. 7a** shows the best catalytic performance just before catalyst degradation for different temperatures. The higher the temperature, the shorter the reaction time and the lower conversion and selectivity. We conclude that 60 °C / 24 h is the optimum reaction condition without catalyst degradation. **Fig. 7b** shows the results of adding extra solvent (1 mL) to the reaction medium. Performance is significantly lower in the presence of acetonitrile, and even poorer with additional water. By varying the amount of the substrate from 1 to 3 mmol, we can see from **Fig. 7c** that the lower the amount, the higher the catalytic performance, achieving full conversion and selectivity at 1.5 mmol BnOH. The kinetic study is therefore carried out with this optimal amount of substrate and illustrated in **Fig. 7d**. The reaction gets off to a slow start since it is only after 7 h of reaction that significant conversion is recorded with very low selectivity (< 50%), meaning that the prominent product at this stage is benzaldehyde. This proves that the oxidation to benzoic acid is a two-step process via benzaldehyde. Finally, tests on the recyclability of the catalyst recovered by simple separation of the reaction mixture by centrifugation are shown in **Fig. 7e** and **7f**. The same starting catalyst was successfully used up to five runs. During the first three cycles there is no apparent degradation of the catalyst, the liquid part of the reaction medium was colorless and there was no weight loss of the recovered solid (**Fig. 7f**). Nevertheless, there is a slight, steady decline in performance. After the fourth run, we observe a significant drop in conversion and selectivity as a result of catalyst degradation, observed by a 20% weight loss and the yellow product coloring (see **Fig. 8f** and next section). After the five runs, only 15% of the initial catalyst is recovered due to advanced oxidation of the polymer backbone, despite the preservation of a certain catalytic performance.

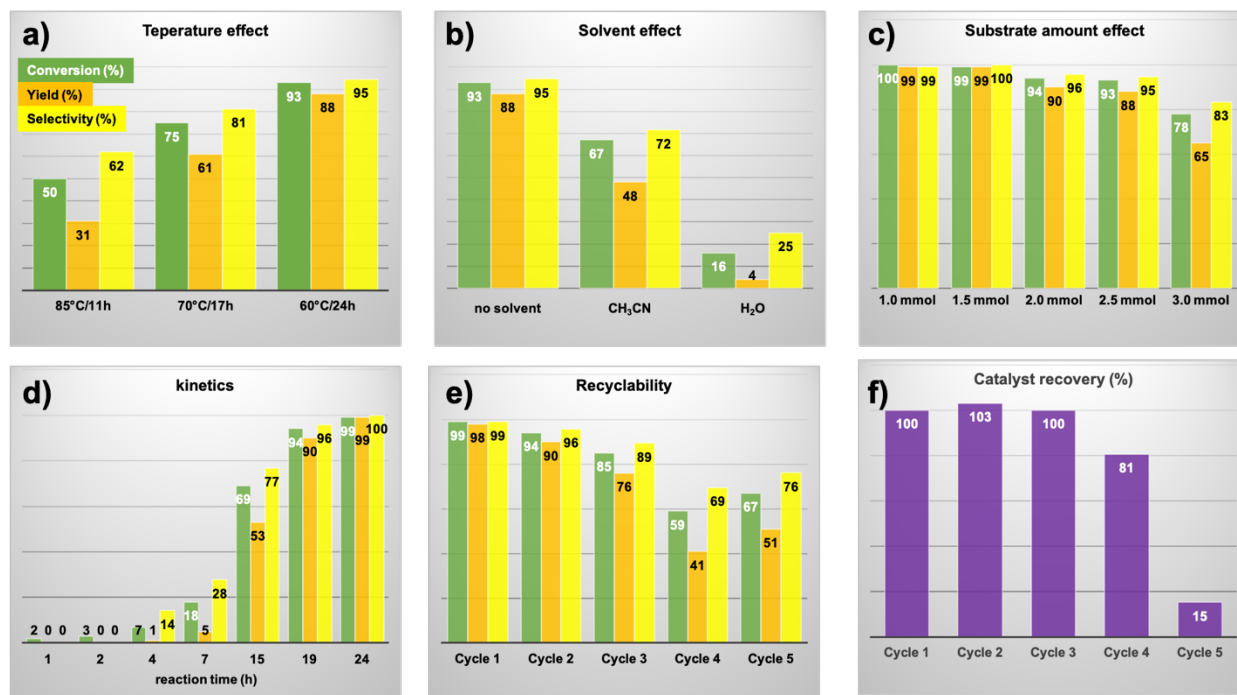


**Fig. 7:** Oxidation of benzyl alcohol to benzoic acid with  $\{PV^{IV}W_{11}\}^{5-}@CD-EPI$  using *t*-BuOOH as oxidizing agent: a) temperature effect, b) solvent effect, c) substrate amount effect, d) kinetic study, and e-f) recyclability study. Reaction conditions when not indicated: 2.5 mmol substrate in a) and b) or 1.5 mmol substrate in d) and e-f), 12.5 mmol oxidizing agent, 0.01 mmol POM, 1 mL solvent, 60 °C, 24 h.

In summary, our  $\{PV^{IV}W_{11}\}^{5-}@CD-EPI$  composite exhibits excellent catalytic activity for the oxidation of benzyl alcohol to benzoic acid with *t*-BuOOH and can be compared with other reported tungsten-POM based catalysts (**Table 6**). In comparison with the literature, only two systems showed such good results for benzoic acid as the final product. The former is a silver-containing POM framework effective under aerobic conditions in photocatalysis,<sup>67</sup> while the latter is a supramolecular complex with  $\beta$ -CD  $\{3CD@SiW_{12}\}$  used in  $H_2O_2$ .<sup>25</sup> The TON and TOF values of 125 and  $5\text{ h}^{-1}$ , respectively, for our  $\{PV^{IV}W_{11}\}^{5-}@CD-EPI$  catalyst are within the typical ranges reported. Most other work on this catalysis has reported rather high selectivity for benzaldehyde.<sup>68–74</sup> We also note that  $H_2O_2$  is the oxidizing agent most commonly used for this reaction, and that the temperature is generally high, between 85 and 110 °C. Although the most widely used tungsten-based Keggin catalysts are phosphododecatungstate  $\{PW_{12}\}$ , a few

examples of mixed vanadotungstate POMs have also been reported in the catalytic oxidation of benzyl alcohol.<sup>75–78</sup> In all these studies, selectivity was once again exclusive to benzaldehyde.

**Table 6:** Comparison with the literature of the performance of the  $\{PV^{IV}W_{11}\}^{5-}@CD-EPI$  catalyst in the oxidation of benzyl alcohol (BnOH) to benzoic acid (BzOH)

Catalyst	Oxidant	T (°C)/t (h)	Conversion (%)	Selectivity BzOH (%)	TON <sup>a</sup>	TOF <sup>b</sup> (h <sup>-1</sup> )	Reference
$\{PV^{IV}W_{11}\}^{5-}@CD-EPI$	t-BuOOH	60 °C/24 h	99	100	124	5	This work
$[Ag_3L_2(OH)]\{PW_{12}\}^c$	$\lambda$ 365 nm <sup>g</sup>	RT /12 h	99	99	10	1	67
$\{3CD@SiW_{12}\}$	H <sub>2</sub> O <sub>2</sub>	85 °C/24 h	96	97	233	10	25
$[L]_7\{PW_{11}\}^d$	H <sub>2</sub> O <sub>2</sub>	85 °C/7 h	99	58	72	10	79
$\{NiSiW_{12}\}$	H <sub>2</sub> O <sub>2</sub>	90 °C/3.5 h	34	38	37	10	69
$\{PW_{12}\}@MC^e$	H <sub>2</sub> O <sub>2</sub>	95 °C/5 h	92	31	36	7	70
Ce <sub>0.66</sub> H $\{PW_{12}\}$	H <sub>2</sub> O <sub>2</sub>	110 °C/4 h	96	26	173	43	73
MimAM(H)- $\{PW_{12}\}^f$	H <sub>2</sub> O <sub>2</sub>	90 °C/0.5 h	100	17	53	106	72
$\{BW_{11}\}$	H <sub>2</sub> O <sub>2</sub>	90 °C/6 h	98	16	10	2	68
Py <sub>3</sub> $\{PW_{12}\}$	H <sub>2</sub> O <sub>2</sub>	90 °C/2 h	33	19	21	10	71
H <sub>3</sub> $\{PW_{12}\}$	H <sub>2</sub> O <sub>2</sub>	90 °C/15 h	96	10	19	1	74

a) TON = moles of BzOH produced/moles of POM, b) TOF = TON / t (h), c) L = 1,4-di(4H-1,2,4-triazol-4-yl), d) L = N(C<sub>18</sub>H<sub>37</sub>)<sub>2</sub>(CH<sub>3</sub>)<sub>2</sub>, e) MC = mesoporous carbon, f) MimAM = 1-aminoethyl-3-methylimidazolium, g) photocatalysis.

### Stability of POM@CD-EPI composites during catalysis

To gain further insights into the stability of the composite after catalysis, NMR analyses of the catalyst and the reaction medium were performed after successive cycles, as shown in **Fig. 8**. Solid state NMR spectra (<sup>51</sup>V and <sup>31</sup>P) of the catalyst before and after one and five uses showed identical spectra indicating the preservation of the integrity of the POM structure in the composite throughout the five catalytic cycles. In <sup>13</sup>C NMR, we also observe the same resonances of the starting polymer, again indicating no major deterioration of the polymer matrix. We observe, however, small additional resonances due to the presence of residual reactants and products still absorbed, e.g., t-BuOOH/t-BuOH, BnOH, BzOH. This may explain the slight increase in recovered catalyst weight in some cases exceeding 100% recovery (**Fig. 7f**). These results confirm the relative robustness of the composite and its resistance to the catalysis conditions

studied (t-BuOOH, 60 °C / 24 h). In the liquid phase no signals were detected in  $^{51}\text{V}$  or  $^{31}\text{P}$  NMR up to three cycles (Fig. 8d and 8e), but the POM  $\{\text{PV}^{\text{V}}\text{W}_{11}\}^{4-}$  resonances start to appear in the fourth cycle and continue to increase in the fifth cycle. ICP analyses are also consistent with POM leaching only after four catalytic cycles (see Table S3, ESI<sup>†</sup>). This is consistent with the yellowish color of the products observed beyond the fourth cycle (Fig. 8f) and also with the previous catalytic results (Fig. 7f and 7e). This means that the deterioration results from leaching of the POM units, most likely following the degradation of the polymer backbone which also contains alcohol functions (from cyclodextrin and glycerol moieties) and is therefore subject to oxidative attack. It is worth noting that, when using  $\text{H}_2\text{O}_2$  or POM as a catalyst instead of composite, the POM is degraded and other species are formed (see Fig. S15c and S15d, ESI<sup>†</sup>).

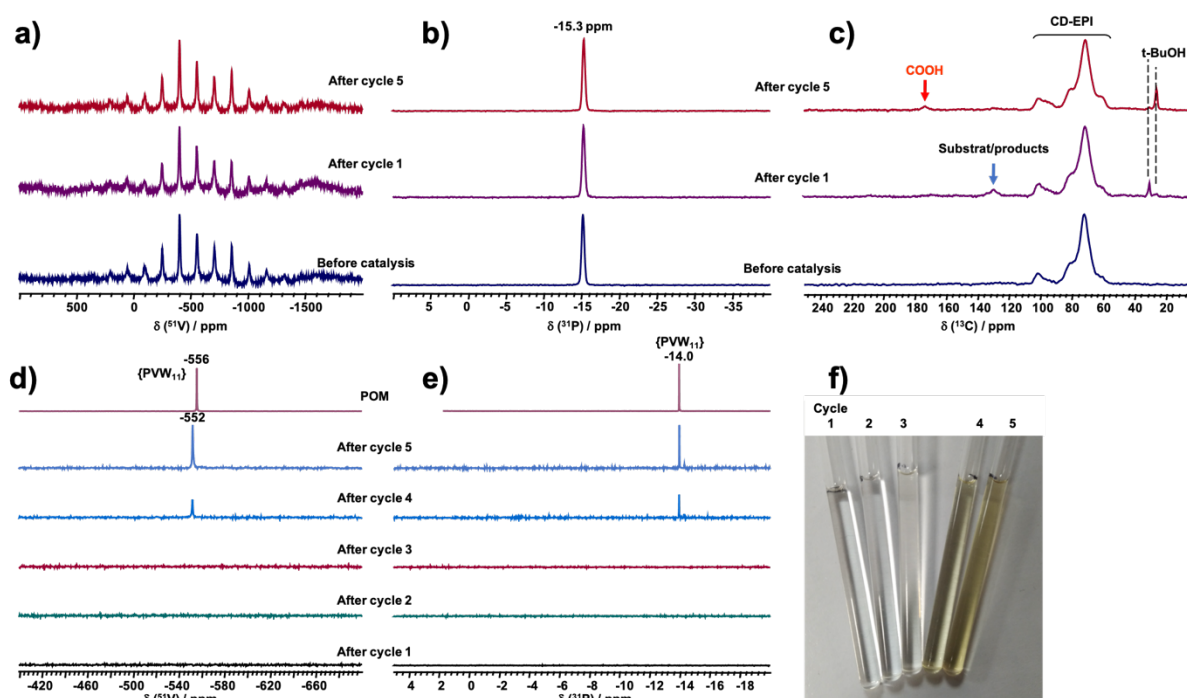


**Fig. 8:** Solid state a)  $^{51}\text{V}$  MAS, b)  $^{31}\text{P}$  MAS, and c)  $^{13}\text{C}\{^1\text{H}\}$  CPMAS NMR spectra of catalyst before ( $\{\text{PV}^{\text{V}}\text{W}_{11}\}^{4-}$  @CD-EPI) and after catalysis ( $\{\text{PV}^{\text{IV}}\text{W}_{11}\}^{5-}$  @CD-EPI). Liquid state d)  $^{51}\text{V}$  and e)  $^{31}\text{P}$  NMR spectra of liquid part of reaction medium in  $\text{CD}_3\text{CN}$  compared to spectra of starting POM  $\text{K}_4[\text{PV}^{\text{V}}\text{W}_{11}\text{O}_{40}]$  in  $\text{D}_2\text{O}$ . f) photographs of the NMR tubes of d) and f). Reaction conditions of one cycle: 1.5 mmol substrate, 12.5 mmol oxidizing agent t-BuOOH, 0.01 mmol POM in catalyst, 60 °C, 24 h.

## Mechanisms and reaction pathways

On the basis of the experimental results and observations made above, we propose in **Fig. 9** mechanisms based on the unique host-guest supramolecular property of CD to explain the remarkable catalytic activity of our POM@CD-EPI composite with the oxidizing agent t-BuOOH regarding i) its structural stability and integrity, and ii) its selectivity for the oxidation of benzyl alcohol to benzoic acid. The key point here is the hydrophobic bulky character of the tert-butyl moiety of the oxidizing agent. First concerning the stability of the composite (**Fig. 9a**), in the presence of CD-based polymer, t-BuOOH should be adsorbed specifically into the CD cavity governed by a hydrophobic attraction driving force.  $^{13}\text{C}$  NMR (**Fig. 8c**) showed indeed the adsorption of some t-BuOOH/t-BuOH in the catalyst. The CD/POM molar ratio is about five, suggesting that the composite should contain many free CDs as potential interaction sites. Moreover, the hydrophobic character of t-BuOOH can prevent its approach to the organic part (polymer backbone) of the composite, while this is not the case of the smaller and hydrophilic  $\text{H}_2\text{O}_2$ . The oxidative attack of the latter of the numerous hydroxyl groups of the glycerol fragments then becomes very favorable, thus weakening the polymer matrix of the composite and therefore the fixation of the POM. Therefore, the use of a weak oxidant like t-BuOOH becomes advantageous here to avoid overoxidation of the polymer.

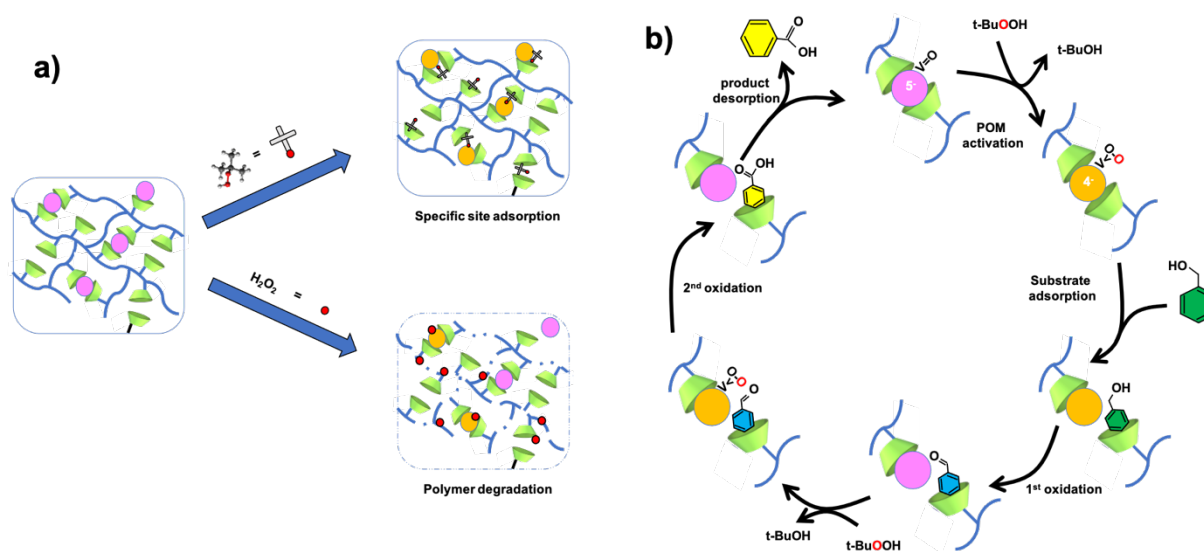


**Fig. 9:** Proposed mechanisms based on the host-guest supramolecular effect of CD to a) avoid degradation of the polymer backbone and to b) drive oxidation process of BnOH selectively to BzOH.

Once adsorbed, t-BuOOH must be sufficiently close to the POM deeply embedded in the polymer matrix, thus facilitating its activation. For that t-BuOOH needs to diffuse into the polymer matrix of the composite, which explains the induction time of 2-4 h observed in the kinetic study (Fig. 7d). In addition, solid-state NMR of the recovered catalyst, shown in Fig. 8c, also indicates the presence of occluded t-BuOOH/t-BuOH species despite intensive washing. Fig. 9b schematically shows the catalytic cycle taking place inside the POM-polymer composite. It is well established that vanadium plays a key role in the activation of POM by increasing its redox potentials.<sup>78</sup> The postulated active species is therefore a vanadoperoxo complex that provides active oxygen.<sup>80,81</sup> Because cyclodextrins constitute the anchoring sites of the POM species but also the oxidizing agent, the catalytic process is governed as a whole by supramolecular chemistry and reactions in confined environment. Indeed, the diffusion and molecular approach of the substrate should occur through its hydrophobic part, i.e., its aromatic ring, to form host-guest complexes with the central cavity of CDs without dissociating the POMs from the polymer host. The simultaneous process of complexation and oxidation of substrates taking place inside the POM-polymer composite in a confined environment is expected to be much more efficient than catalysis with separately free CD and POM molecular constituents. This may explain why a second consecutive oxidation occurs immediately after the first one to produce the final benzoic acid product. Confined reactions have several advantages, including i) acceleration of the catalytic process by favorizing molecular contact and, more interestingly, ii) promotion of cascade reactions through steric effect which improves selectivity. It appears that the beneficial role of CD lies in its ability to promote supramolecular complexation not only with organic molecules (t-BuOOH and substrate) through its well-known hydrophobic effect, but also with inorganic POM through its newly discovered chaotropic effect.

## Conclusions

In this research, we present a detailed quantitative study of the adsorption process of polyoxometalates on a  $\gamma$ -CD-based polymer, including adsorption isotherms and kinetics. The polymer resulting from the copolymerization of  $\gamma$ -CD with EPI showed high affinity towards POMs

of the Keggin structure. The integrity of the POM structure and the preservation of its chemical composition in the hybrids were verified using solid-state NMR, FT-IR spectroscopy and elemental analyses. The maximum adsorption capacity ( $q_{\max}$ ) was estimated between 75 to 135  $\mu\text{mol.g}^{-1}$ , depending on the negative charge of the POM, i.e., the lower the charge, the higher the  $q_{\max}$ . Such a trend suggests an adsorption mechanism driven by the chaotropic effect, where the solvation properties of POM depend strongly on the charge density at its surface. These  $q_{\max}$  values match the typical adsorption performance observed with mesoporous such as MOFs. The potential of CD-EPI polymers as alternative supports for POM heterogenization is evaluated in the selective oxidation of benzyl alcohol. The bulky and hydrophobic oxidizing agent t-BuOOH was found to be the best partner of  $\{\text{PVW}_{11}\}^{5/4-}$ @CD-EPI to form an efficient catalyst tandem for the oxidation of benzyl alcohol to benzoic acid. The host-guest supramolecular properties of CD are key parameters not only to improve the catalyst stability but also the catalytic performances through reactions in a confined environment. With these promising results, our team is now focusing on using the  $\gamma$ -CD-based polymer as a hosting matrix to entrap complementary functional building units to design photo-catalytic systems or tandem catalysis.

## Data availability

The authors confirm that the data supporting the findings of this study are available within the article and its ESI<sup>†</sup>.

## Conflicts of interest

There are no conflicts to declare.

## Acknowledgement

This work is supported by the “Investissements d’Avenir” program (Labex Charm3at, ANR-11-LABX-0039-grant). The CNRS and the University of Versailles Saint-Quentin are acknowledged for

their financial supports. The Authors thank Dr. Ruxandra Gref from the Université Paris-Saclay for her advice on the synthesis of CD-EPI based polymers. SA thanks CampusFrance for the Excellence Eiffel doctoral grant.

## References

- (1) Gumerova, N. I.; Rompel, A. Polyoxometalates in Solution: Speciation under Spotlight. *Chem. Soc. Rev.* **2020**, *49* (21), 7568–7601. <https://doi.org/10.1039/d0cs00392a>.
- (2) Maalaoui, A.; Guedidi, H.; Rzaigui, M.; Akriche, S. Aldehyde-Assisted Aerobic-Oxidative Desulfurization of HDS Diesel Fuels by a Highly Effective Heterogeneous V-Substituted Keggin-Type Semiorganic Catalyst: Modeling of Experimental Design and Mechanistic and Kinetic Insights. *Energy Fuels* **2024**, *38* (2), 1319–1329. <https://doi.org/10.1021/acs.energyfuels.3c04332>.
- (3) Nakagawa, Y.; Kamata, K.; Kotani, M.; Yamaguchi, K.; Mizuno, N. Polyoxovanadometalate-Catalyzed Selective Epoxidation of Alkenes with Hydrogen Peroxide. *Angew. Chem. Int. Ed.* **2005**, *44* (32), 5136–5141. <https://doi.org/10.1002/anie.200500491>.
- (4) Petel, B. E.; Matson, E. M. Oxygen-Atom Vacancy Formation and Reactivity in Polyoxovanadate Clusters. *Chem. Commun.* **2020**, *56* (88), 13477–13490. <https://doi.org/10.1039/D0CC05920J>.
- (5) Seki, Y.; Mizuno, N.; Misono, M. Catalytic Performance of 11-Molybdo-1-Vanadophosphoric Acid as a Catalyst Precursor and the Optimization of Reaction Conditions for the Oxidation of Methane with Hydrogen Peroxide. *Appl. Catal. A-Gen.* **2000**, *194–195*, 13–20. [https://doi.org/10.1016/S0926-860X\(99\)00348-8](https://doi.org/10.1016/S0926-860X(99)00348-8).
- (6) Anyushin, A.; Kondinski, A.; Parac-Vogt, T. N. Hybrid Polyoxometalates as Post-Functionalization Platforms: From Fundamentals to Emerging Applications. *Chem. Soc. Rev.* **2020**, *49* (2), 382–432. <https://doi.org/10.1039/c8cs00854j>.
- (7) Ebrahimi, A.; Krivosudsky, L.; Cherevan, A.; Eder, D. Polyoxometalate-Based Porphyrinic Metal-Organic Frameworks as Heterogeneous Catalysts. *Coord. Chem. Rev.* **2024**, *508*, 215764. <https://doi.org/10.1016/j.ccr.2024.215764>.
- (8) Kawahara, R.; Niinomi, K.; Kondo, J. N.; Hibino, M.; Mizuno, N.; Uchida, S. A Functional Mesoporous Ionic Crystal Based on Polyoxometalate. *Dalton Trans.* **2016**, *45* (7), 2805–2809. <https://doi.org/10.1039/C5DT04556H>.
- (9) Martinetto, Y.; Pegot, B.; Roch-Marchal, C.; Cottyn-Boitte, B.; Floquet, S. Designing Functional Polyoxometalate-Based Ionic Liquid Crystals and Ionic Liquids. *Eur. J. Inorg. Chem.* **2019**, *21*. <https://doi.org/10.1002/ejic.201900990>.
- (10) Ma, P.; Hu, F.; Wang, J.; Niu, J. Carboxylate Covalently Modified Polyoxometalates: From Synthesis, Structural Diversity to Applications. *Coord. Chem. Rev.* **2019**, *378*, 281–309. <https://doi.org/10.1016/j.ccr.2018.02.010>.

- (11) Stracke, J. J.; Finke, R. G. Distinguishing Homogeneous from Heterogeneous Water Oxidation Catalysis When Beginning with Polyoxometalates. *ACS Catal.* **2014**, *4* (3), 909–933. <https://doi.org/10.1021/cs4011716>.
- (12) Chen, G.; Zhou, Y.; Long, Z.; Wang, X.; Li, J.; Wang, J. Mesoporous Polyoxometalate-Based Ionic Hybrid As a Triphasic Catalyst for Oxidation of Benzyl Alcohol with H<sub>2</sub>O<sub>2</sub> on Water. *ACS Appl. Mater. Interfaces* **2014**, *6* (6), 4438–4446. <https://doi.org/10.1021/am5001757>.
- (13) Maru, K.; Kalla, S.; Jangir, R. MOF/POM Hybrids as Catalysts for Organic Transformations. *Dalton Trans.* **2022**, *51*, 11952–11986. <https://doi.org/10.1039/d2dt01895k>.
- (14) Misra, A.; Franco Castillo, I.; Müller, D. P.; González, C.; Eyssautier-Chuine, S.; Ziegler, A.; de la Fuente, J. M.; Mitchell, S. G.; Streb, C. Polyoxometalate-Ionic Liquids (POM-ILs) as Anticorrosion and Antibacterial Coatings for Natural Stones. *Angew. Chem. Int. Ed.* **2018**, *57* (45), 14926–14931. <https://doi.org/10.1002/anie.201809893>.
- (15) Sun, J.; Abednatanzi, S.; Van Der Voort, P.; Liu, Y.-Y.; Leus, K. POM@MOF Hybrids: Synthesis and Applications. *Catalysts* **2020**, *10* (5), 578. <https://doi.org/10.3390/catal10050578>.
- (16) Ullah, I.; Munir, A.; Haider, A.; Ullah, N.; Hussain, I. Supported Polyoxometalates as Emerging Nanohybrid Materials for Photochemical and Photoelectrochemical Water Splitting. *Nanophotonics* **2021**, *10* (6), 1595–1620. <https://doi.org/10.1515/nanoph-2020-0542>.
- (17) Simons, J.; Hazra, N.; Petrunin, A. V.; Crassous, J. J.; Richtering, W.; Hohenschutz, M. Nonionic Microgels Adapt to Ionic Guest Molecules: Superchaotropic Nanoions. *ACS Nano* **2024**, *18*, 7546–7557. <https://doi.org/10.1021/acsnano.3c12357>.
- (18) Mu, C.; Chen, Y.; Dai, Z.; Li, W.; Wang, J.; Jiao, X.; Chen, D.; Wang, T. Pom Functionalized Ionogels with Tunable Optical, Mechanical, Electrical, and Sensory Properties. *Adv. Funct. Mater.* **2023**, 2313957. <https://doi.org/10.1002/adfm.202313957>.
- (19) Salomon, W.; Lan, Y. H.; Riviere, E.; Yang, S.; Roch-Marchal, C.; Dolbecq, A.; Simonnet-Jegat, C.; Steunou, N.; Leclerc-Laronze, N.; Ruhlmann, L.; Mallah, T.; Wernsdorfer, W.; Mialane, P. Single-Molecule Magnet Behavior of Individual Polyoxometalate Molecules Incorporated within Biopolymer or Metal-Organic Framework Matrices. *Chem.-Eur. J.* **2016**, *22* (19), 6564–6574. <https://doi.org/10.1002/chem.201600202>.
- (20) Yao, S.; Falaise, C.; Ivanov, A. A.; Leclerc, N.; Hohenschutz, M.; Haouas, M.; Landy, D.; Shestopalov, M. A.; Bauduin, P.; Cadot, E. Hofmeister Effect in the Keggin-Type Polyoxotungstate Series. *Inorg. Chem. Front.* **2021**, *8* (1), 12–25. <https://doi.org/10.1039/d0qi00902d>.
- (21) Khelifi, S.; Yao, S.; Falaise, C.; Bauduin, P.; Guerineau, V.; Leclerc, N.; Haouas, M.; Salmi-Mani, H.; Roger, P.; Cadot, E. Switchable Redox and Thermo-Responsive Supramolecular Polymers Based on Cyclodextrin-Polyoxometalate Tandem. *Chem.-Eur. J.* **2024**, *30*, e202303815. <https://doi.org/10.1002/chem.202303815>.
- (22) Yao, S.; Falaise, C.; Leclerc, N.; Roch-Marchal, C.; Haouas, M.; Cadot, E. Improvement of the Hydrolytic Stability of the Keggin Molybdo- and Tungsto-Phosphate Anions by Cyclodextrins. *Inorg. Chem.* **2022**, *61* (9), 4193–4203. <https://doi.org/10.1021/acs.inorgchem.2c00095>.
- (23) Fan, Y.; Zhang, Y.; Jia, Q.; Cao, J.; Wu, W. The Stabilizing Role of Cyclodextrins on Keggin Phosphotungstic Acid by Complexation Unveiled by Electrospray Mass Spectrometry. *Mass Spectrom. Lett.*

**2015**, 6 (1), 13–16. <https://doi.org/10.5478/MSL.2015.6.1.13>.

(24) Zhu, Z.; Wei, M.; Li, B.; Wu, L. Constructing Chiral Polyoxometalate Assemblies via Supramolecular Approaches. *Dalton Trans.* **2021**, 50 (15), 5080–5098. <https://doi.org/10.1039/d1dt00182e>.

(25) Ni, L.; Li, H.; Xu, H.; Shen, C.; Liu, R.; Xie, J.; Zhang, F.; Chen, C.; Zhao, H.; Zuo, T.; Diao, G. Self-Assembled Supramolecular Polyoxometalate Hybrid Architecture as a Multifunctional Oxidation Catalyst. *ACS Appl. Mater. Interfaces* **2019**, 11 (42), 38708–38718. <https://doi.org/10.1021/acsami.9b12531>.

(26) Khlifi, S.; Marrot, J.; Haouas, M.; Shepard, W. E.; Falaise, C.; Cadot, E. Chaotropic Effect as an Assembly Motif to Construct Supramolecular Cyclodextrin-Polyoxometalate-Based Frameworks. *J. Am. Chem. Soc.* **2022**, 144 (10), 4469–4477. <https://doi.org/10.1021/jacs.1c12049>.

(27) Yang, P.; Zhao, W.; Shkurenko, A.; Belmabkhout, Y.; Eddaoudi, M.; Dong, X.; Alshareef, H. N.; Khashab, N. M. Polyoxometalate-Cyclodextrin Metal-Organic Frameworks: From Tunable Structure to Customized Storage Functionality. *J. Am. Chem. Soc.* **2019**, 141 (5), 1847–1851. <https://doi.org/10.1021/jacs.8b11998>.

(28) Gidwani, B.; Vyas, A. A Comprehensive Review on Cyclodextrin-Based Carriers for Delivery of Chemotherapeutic Cytotoxic Anticancer Drugs. *Biomed. Res. Int.* **2015**, 98268. <https://doi.org/10.1155/2015/198268>.

(29) Komiyama, M. Monomeric, Oligomeric, Polymeric, and Supramolecular Cyclodextrins as Catalysts for Green Chemistry. *Research* **2024**, 7, 0466. <https://doi.org/10.34133/research.0466>.

(30) Liu, X.; Zhang, J.; Lan, Y.; Zheng, Q.; Xuan, W. Infinite Building Blocks for Directed Self-Assembly of a Supramolecular Polyoxometalate-Cyclodextrin Framework for Multifunctional Oxidative Catalysis. *Inorganic Chemistry Frontiers* **2022**. <https://doi.org/10.1039/d2qi02085h>.

(31) Sadjadi, S.; Rezadoust, A. M.; Yaghoubi, S.; Monflier, E.; Heydari, A. 3D-Printed Cyclodextrin Polymer Encapsulated Wells-Dawson: A Novel Catalyst for Knoevenagel Condensation Reactions. *ACS Omega* **2023**, 8 (48), 45844–45853. <https://doi.org/10.1021/acsomega.3c06592>.

(32) Falaise, C.; Khlifi, S.; Bauduin, P.; Schmid, P.; Degrouard, J.; Leforestier, A.; Shepard, W.; Marrot, J.; Haouas, M.; Landy, D.; Mellot-Draznieks, C.; Cadot, E. Cooperative Self-Assembly Process Involving Giant Toroidal Polyoxometalate as a Membrane Building Block in Nanoscale Vesicles. *J. Am. Chem. Soc.* **2024**, 146 (2), 1501–1511. <https://doi.org/10.1021/jacs.3c11004>.

(33) Hohenschutz, M.; Bauduin, P.; Lopez, C. G.; Foerster, B.; Richtering, W. Superchaotropic Nano-Ion Binding as a Gelation Motif in Cellulose Ether Solutions. *Angewandte Chemie-International Edition* **2023**. <https://doi.org/10.1002/anie.202210208>.

(34) Malinenko, A.; Jonchère, A.; Girard, L.; Parrès-Maynadié, S.; Diat, O.; Bauduin, P. Are Keggin's POMs Charged Nanocolloids or Multicharged Anions? *Langmuir* **2018**, 34 (5), 2026–2038. <https://doi.org/10.1021/acs.langmuir.7b03640>.

(35) Romo, A.; Peñas, F. J.; Sevillano, X.; Isasi, J. R. Application of Factorial Experimental Design to the Study of the Suspension Polymerization of  $\beta$ -Cyclodextrin and Epichlorohydrin. *J. Appl. Polym. Sci.* **2006**, 100 (4), 3393–3402. <https://doi.org/10.1002/app.23778>.

(36) Renard, E.; Deratani, A.; Volet, G.; Sebillé, B. Preparation and Characterization of Water Soluble

High Molecular Weight Beta-Cyclodextrin-Epichlorohydrin Polymers. *Eur. Polym. J.* **1997**, *33* (1), 49–57. [https://doi.org/10.1016/S0014-3057\(96\)00123-1](https://doi.org/10.1016/S0014-3057(96)00123-1).

(37) Crini, G.; Cosentino, C.; Bertini, S.; Naggi, A.; Torri, G.; Vecchi, C.; Janus, L.; Morcellet, M. Solid State NMR Spectroscopy Study of Molecular Motion in Cyclomaltoheptaose ( $\beta$ -Cyclodextrin) Crosslinked with Epichlorohydrin. *Carbohydr. Res.* **1998**, *308* (1–2), 37–45. [https://doi.org/10.1016/S0008-6215\(98\)00077-9](https://doi.org/10.1016/S0008-6215(98)00077-9).

(38) Mallard, I.; Baudelet, D.; Castiglione, F.; Ferro, M.; Panzeri, W.; Ragg, E.; Mele, A. Polydisperse Methyl  $\beta$ -Cyclodextrin-Epichlorohydrin Polymers: Variable Contact Time  $^{13}\text{C}$  CP-MAS Solid-State NMR Characterization. *Beilstein J. Org. Chem.* **2015**, *11*, 2785–2794. <https://doi.org/10.3762/bjoc.11.299>.

(39) Pellicer, J. A.; Rodriguez-Lopez, M. I.; Fortea, M. I.; Gomez-Lopez, V. M.; Aunon, D.; Nunez-Delicado, E.; Gabaldon, J. A. Synthesis of New Cyclodextrin-Based Adsorbents to Remove Direct Red 83:1. *Polymers* **2020**, *12* (9), 1880. <https://doi.org/10.3390/polym12091880>.

(40) Rusu, D.; Baban, O.; Hauer, I.; Gligor, D.; David, L.; Rusu, M. Synthesis and Characterization of the Potassium 11-Tungstovanado(IV) Phosphate. *Rev. Roum. Chim.* **2010**, *55* (11–12), 843–850.

(41) Lu, X.; Cheng, T.; Geletii, Y. V.; Bacsá, J.; Hill, C. L. Reactivity and Stability Synergism Directed by the Electron Transfer between Polyoxometalates and Metal-Organic Frameworks. *Catal. Sci. Technol.* **2023**, *13*, 5094–5103. <https://doi.org/10.1039/d3cy00569k>.

(42) Ho, Y.-S. Review of Second-Order Models for Adsorption Systems. *J. Hazard. Mater.* **2006**, *136* (3), 681–689. <https://doi.org/10.1016/j.jhazmat.2005.12.043>.

(43) Wang, J.; Guo, X. Adsorption Kinetic Models: Physical Meanings, Applications, and Solving Methods. *J. Hazard. Mater.* **2020**, *390*, 122156. <https://doi.org/10.1016/j.jhazmat.2020.122156>.

(44) Pellicer, J. A.; Isabel Rodriguez-Lopez, M.; Fortea, M. I.; Gabaldon Hernandez, J. A.; Lucas-Abellan, C.; Teresa Mercader-Ros, M.; Serrano-Martinez, A.; Nunez-Delicado, E.; Cosma, P.; Fini, P.; Franco, E.; Garcia, R.; Ferrandiz, M.; Perez, E.; Ferrandiz, M. Removing of Direct Red 83:1 Using  $\alpha$ - and HP- $\alpha$ -CDs Polymerized with Epichlorohydrin: Kinetic and Equilibrium Studies. *Dyes Pigment.* **2018**, *149*, 736–746. <https://doi.org/10.1016/j.dyepig.2017.11.032>.

(45) Rocchiccioli-Deltcheff, C.; Fournier, M.; Franck, R.; Thouvenot, R. Vibrational Investigations of Polyoxometalates .2. Evidence for Anion-Anion Interactions in Molybdenum(VI) and Tungsten(VI) Compounds Related to the Keggin Structure. *Inorg. Chem.* **1983**, *22* (2), 207–216. <https://doi.org/10.1021/ic00144a006>.

(46) Canioni, R.; Roch-Marchal, C.; Haouas, M.; Vimont, A.; Horcajada, P.; Sécheresse, F.; Serre, C. MIL-101(Cr) MOF as a Support for Reactive Polyoxometalates (POMs) Clusters. Principles of POMs Encapsulation and Chemistry of POMs Inside MIL-101 Cavities. *Current Inorganic Chemistry*, 2017, *7*, 145–156. <https://doi.org/10.2174/1877944107666171102141415>.

(47) Juan-Alcaniz, J.; Goesten, M. G.; Ramos-Fernandez, E. V.; Gascon, J.; Kapteijn, F. Towards Efficient Polyoxometalate Encapsulation in MIL-100(Cr): Influence of Synthesis Conditions. *New J. Chem.* **2012**, *36* (4), 977–987. <https://doi.org/10.1039/c2nj20587d>.

(48) Bonfim, R. de P. F.; de Moura, L. C.; Pizzala, H.; Caldarelli, S.; Paul, S.; Eon, J. G.; Mentre, O.; Capron, M.; Delevoye, L.; Payen, E. Synthesis and Structural Characterization of a New Nanoporous-like

Keggin Heteropolyanion Salt:  $K_3(H_2O)_4[H_2SiVW_{11}O_{40}](H_2O)_{8+x}$ . *Inorg. Chem.* **2007**, *46* (18), 7371–7377. <https://doi.org/10.1021/ic700384m>.

(49) Massiot, D.; Fayon, F.; Capron, M.; King, I.; Le Calve, S.; Alonso, B.; Durand, J.; Bujoli, B.; Gan, Z.; Hoatson, G. Modelling One- and Two-Dimensional Solid-State NMR Spectra. *Magn. Reson. Chem.* **2002**, *40* (1), 70–76. <https://doi.org/10.1002/mrc.984>.

(50) Schwegler, M.; Vinke, P.; Van Derwijk, M.; Van Bekkum, H. Activated Carbon as a Support For Heteropolyanion Catalysts. *Appl. Catal. A-Gen.* **1992**, *80* (1), 41–57. [https://doi.org/10.1016/0926-860X\(92\)85107-M](https://doi.org/10.1016/0926-860X(92)85107-M).

(51) Castillo, M. A.; Vazquez, P. G.; Blanco, M. N.; Caceres, C. V. Adsorption Studies and Species Characterization in Catalysts Obtained from Aqueous Solutions of Phosphomolybdic Acid and Gamma-Alumina. *J. Chem. Soc.-Faraday Trans.* **1996**, *92* (17), 3239–3246. <https://doi.org/10.1039/ft9969203239>.

(52) Wu, Y.; Ye, X. K.; Yang, X. G.; Wang, X. P.; Chu, W. L.; Hu, Y. C. Heterogenization of Heteropolyacids: A General Discussion on the Preparation of Supported Acid Catalysts. *Ind. Eng. Chem. Res.* **1996**, *35* (8), 2546–2560. <https://doi.org/10.1021/ie950473s>.

(53) Chu, W. L.; Yang, X. G.; Ye, X. K.; Wu, Y. Adsorption of  $PMo_{12}$  and  $SiMo_{12}$  on Activated Carbon in Aqueous and Acidic Media. *Langmuir* **1996**, *12* (17), 4185–4189. <https://doi.org/10.1021/la950412z>.

(54) Benseghir, Y.; Lemarchand, A.; Duguet, M.; Mialane, P.; Gomez-Mingot, M.; Roch-Marchal, C.; Pino, T.; Ha-Thi, M. H.; Haouas, M.; Fontecave, M.; Dolbecq, A.; Sassoie, C.; Mellot-Draznieks, C. Co-Immobilization of a Rh Catalyst and a Keggin Polyoxometalate in the UiO-67 Zr-Based Metal-Organic Framework: In Depth Structural Characterization and Photocatalytic Properties for  $CO_2$  Reduction. *J. Am. Chem. Soc.* **2020**, *142* (20), 9428–9438. <https://doi.org/10.1021/jacs.0c02425>.

(55) Fahy, K. M.; Sha, F.; Reischauer, S.; Lee, S.; Tai, T.-Y.; Farha, O. K. Role of Metal-Organic Framework Topology on Thermodynamics of Polyoxometalate Encapsulation. *ACS Appl. Mater. Interfaces* **2024**, *16*, 30296–30305. <https://doi.org/10.1021/acsami.4c05016>.

(56) Paille, G.; Gomez-Mingot, M.; Roch-Marchal, C.; Haouas, M.; Benseghir, Y.; Pino, T.; Ha-Thi, M. H.; Landrot, G.; Mialane, P.; Fontecave, M.; Dolbecq, A.; Mellot-Draznieks, C. Thin Films of Fully Noble Metal-Free POM@MOF for Photocatalytic Water Oxidation. *ACS Appl. Mater. Interfaces* **2019**, *11* (51), 47837–47845. <https://doi.org/10.1021/acsami.9b13121>.

(57) Samaniyan, M.; Mirzaei, M.; Khajavian, R.; Eshtiagh-Hosseini, H.; Streb, C. Heterogeneous Catalysis by Polyoxometalates in Metal–Organic Frameworks. *ACS Catal.* **2019**, *9* (11), 10174–10191. <https://doi.org/10.1021/acscatal.9b03439>.

(58) Ullah, I.; ul Haq, T.; Khan, A. A.; Inayat, A.; Shoaib, M.; Haider, A.; Saleem, M.; Abbas, S. M.; Pope, M. A.; Hussain, I. Sodium Decavanadate Encapsulated Mn-BTC POM@MOF as High-Capacity Cathode Material for Aqueous Sodium-Ion Batteries. *J. Alloy. Compd.* **2023**, *932*, 167647. <https://doi.org/10.1016/j.jallcom.2022.167647>.

(59) Wang, J.; Li, L.; Liu, Y.; Yuan, Z.; Meng, S.; Ma, P.; Wang, J.; Niu, J. Intensifying Photocatalytic Baeyer-Villiger Oxidation of Ketones with the Introduction of Ru Metalloligands and Bimetallic Units in POM@MOF. *Inorg. Chem.* **2024**, *63*, 7325–7333. <https://doi.org/10.1021/acs.inorgchem.4c00217>.

(60) Zhu, T.-T.; Zhang, Z.-M.; Chen, W.-L.; Liu, Z.-J.; Wang, E.-B. Encapsulation of

Tungstophosphoric Acid into Harmless MIL-101(Fe) for Effectively Removing Cationic Dye from Aqueous Solution. *RSC Adv.* **2016**, *6* (85), 81622–81630. <https://doi.org/10.1039/c6ra16716k>.

(61) Ge, Y.; Wang, Y.; Xu, G.; Fang, Z.; Bai, J.; Li, C. Biomass Activated Carbon Supported Keggin-Type Polyoxometalate as an Electrode Material for High-Performance Acidic Aqueous Supercapacitors. *J. Electroanal. Chem.* **2023**, *947*, 117779. <https://doi.org/10.1016/j.jelechem.2023.117779>.

(62) Alcaniz-Monge, J.; Trautwein, G.; Parres-Esclapez, S.; Macia-Agullo, J. A. Influence of Microporosity of Activated Carbons as a Support of Polyoxometalates. *Microporous Mesoporous Mat.* **2008**, *115* (3), 440–446. <https://doi.org/10.1016/j.micromeso.2008.02.017>.

(63) Palomino, P.; Suarez-Guevara, J.; Olivares-Marin, M.; Ruiz, V.; Dubal, D. P.; Gomez-Romero, P.; Tonti, D.; Enciso, E. Influence of Texture in Hybrid Carbon-Phosphomolybdic Acid Materials on Their Performance as Electrodes in Supercapacitors. *Carbon* **2017**, *111*, 74–82. <https://doi.org/10.1016/j.carbon.2016.09.054>.

(64) Duguet, M.; Lemarchand, A.; Benseghir, Y.; Mialane, P.; Gomez-Mingot, M.; Roch-Marchal, C.; Haouas, M.; Fontecave, M.; Mellot-Draznieks, C.; Sassoie, C.; Dolbecq, A. Structure-Directing Role of Immobilized Polyoxometalates in the Synthesis of Porphyrinic Zr-Based Metal-Organic Frameworks. *Chem. Commun.* **2020**, *56* (70), 10143–10146. <https://doi.org/10.1039/d0cc04283h>.

(65) Vázquez, P. G.; Blanco, M. N.; Cáceres, C. V. Catalysts Based on Supported 12-Molybdophosphoric Acid. *Catal. Lett.* **1999**, *60* (4), 205–215. <https://doi.org/10.1023/A:1019071410838>.

(66) Villabrille, P.; Vázquez, P.; Blanco, M.; Cáceres, C. Equilibrium Adsorption of Molybdosilicic Acid Solutions on Carbon and Silica:: Basic Studies for the Preparation of Ecofriendly Acidic Catalysts. *J. Colloid Interface Sci.* **2002**, *251* (1), 151–159. <https://doi.org/10.1006/jcis.2002.8391>.

(67) Zhang, S.-M.; Wang, Y.; Ma, Y.-Y.; Li, Z.-B.; Du, J.; Han, Z.-G. Three-Dimensional Silver-Containing Polyoxotungstate Frameworks for Photocatalytic Aerobic Oxidation of Benzyl Alcohol. *Inorg. Chem.* **2022**. <https://doi.org/10.1021/acs.inorgchem.2c03472>.

(68) Zhao, W.; Zhang, Y.; Ma, B.; Ding, Y.; Qiu, W. Oxidation of Alcohols with Hydrogen Peroxide in Water Catalyzed by Recyclable Keggin-Type Tungstoborate Catalyst. *Catal. Commun.* **2010**, *11* (6), 527–531. <https://doi.org/10.1016/j.catcom.2009.12.010>.

(69) Tian, W.; Hou, Y.; Wang, X.; Lu, B.; Zhao, J.; Cai, Q. A Simple Polyoxometallate for Selective Oxidation of Benzyl Alcohol to Benzaldehyde with Hydrogen Peroxide. *Chin. J. Chem.* **2012**, *30* (2), 433–437. <https://doi.org/10.1002/cjoc.201100144>.

(70) Li, B. L.; Li, J.; Wang, X. M.; Wan, Z. X.; Wang, L. C. Phosphotungstic Acid Supported on Mesoporous Carbon as a Catalyst for the Oxidation of Benzyl Alcohol. *Kinet. Catal.* **2013**, *54* (1), 69–75. <https://doi.org/10.1134/S0023158413010102>.

(71) Leng, Y.; Wang, J.; Jiang, P. Amino-Containing Cross-Linked Ionic Copolymer-Anchored Heteropoly Acid for Solvent-Free Oxidation of Benzyl Alcohol with H<sub>2</sub>O<sub>2</sub>. *Catal. Commun.* **2012**, *27*, 101–104. <https://doi.org/10.1016/j.catcom.2012.07.007>.

(72) Leng, Y.; Liu, J.; Jiang, P.; Wang, J. Heteropolyanion-Based Polymeric Hybrids: Highly Efficient and Recyclable Catalysts for Oxidation of Alcohols with H<sub>2</sub>O<sub>2</sub>. *RSC Adv.* **2012**, *2* (31), 11653–11656. <https://doi.org/10.1039/c2ra22348a>.

- (73) Han, X.; Kuang, Y.; Ouyang, K.; Kan, R.; Tang, X.; Hung, C.-T.; Liu, L.-L.; Wu, P.-H.; Liu, S.-B. Role of Acidity over Rare Earth Metal Ion-Exchanged Heteropoly Tungstates during Oxidation of Alcohols. *J. Taiwan Inst. Chem. Eng.* **2017**, *70*, 23–31. <https://doi.org/10.1016/j.jtice.2016.10.023>.
- (74) Chilivery, R.; Chaitanya, V.; Nayak, J.; Seth, S.; Rana, R. K. Heterogenization of Phosphotungstate Clusters into Magnetic Microspheres: Catalyst for Selective Oxidation of Alcohol in Water. *ACS Sustain. Chem. Eng.* **2022**, *10* (21), 6925–6933. <https://doi.org/10.1021/acssuschemeng.1c07285>.
- (75) Diaz, J.; Pizzio, L. R.; Pecchi, G.; Campos, C. H.; Azocar, L.; Briones, R.; Romero, R.; Henriquez, A.; Gaigneaux, E. M.; Contreras, D. Tetrabutyl Ammonium Salts of Keggin-Type Vanadium-Substituted Phosphomolybdates and Phosphotungstates for Selective Aerobic Catalytic Oxidation of Benzyl Alcohol. *Catalysts* **2022**, *12* (5), 507. <https://doi.org/10.3390/catal12050507>.
- (76) Dong, X.; Wang, D.; Li, K.; Zhen, Y.; Hu, H.; Xue, G. Vanadium-Substituted Heteropolyacids Immobilized on Amine-Functionalized Mesoporous MCM-41: A Recyclable Catalyst for Selective Oxidation of Alcohols with H<sub>2</sub>O<sub>2</sub>. *Mater. Res. Bull.* **2014**, *57*, 210–220. <https://doi.org/10.1016/j.materresbull.2014.05.041>.
- (77) Dong, X.; Zhang, X.; Wu, P.; Zhang, Y.; Liu, B.; Hu, H.; Xue, G. Divanadium-Substituted Phosphotungstate Supported on Magnetic Mesoporous Silica Nanoparticles as Effective and Recyclable Catalysts for the Selective Oxidation of Alcohols. *ChemCatChem* **2016**, *8* (23), 3680–3687. <https://doi.org/10.1002/cctc.201601077>.
- (78) Park, D. R.; Song, S. H.; Hong, U. G.; Seo, J. G.; Jung, J. C.; Song, I. K. Redox Properties and Catalytic Oxidation Activities of Polyatom-Substituted H<sub>n</sub>PW<sub>11</sub>M<sub>1</sub>O<sub>40</sub> (M = V, Nb, Ta, and W) Keggin Heteropolyacid Catalysts. *Catal. Lett.* **2009**, *132* (3–4), 363–369. <https://doi.org/10.1007/s10562-009-0114-9>.
- (79) Ding, Y.; Zhao, W. The Oxidation of Pyridine and Alcohol Using the Keggin-Type Lacunary Polytungstophosphate as a Temperature-Controlled Phase Transfer Catalyst. *J. Mol. Catal. A-Chem.* **2011**, *337* (1–2), 45–51. <https://doi.org/10.1016/j.molcata.2011.01.012>.
- (80) Amitouche, D.; Haouas, M.; Mazari, T.; Mouanni, S.; Canioni, R.; Rabia, C.; Cadot, E.; Marchal-Roch, C. The Primary Stages of Polyoxomolybdate Catalyzed Cyclohexanone Oxidation by Hydrogen Peroxide as Investigated by in Situ NMR. Substrate Activation and Evolution of the Working Catalyst. *Appl. Catal. A-Gen.* **2018**, *561*, 104–116. <https://doi.org/10.1016/j.apcata.2018.05.017>.
- (81) Mizuno, N.; Kamata, K. Catalytic Oxidation of Hydrocarbons with Hydrogen Peroxide by Vanadium-Based Polyoxometalates. *Coord. Chem. Rev.* **2011**, *255* (19–20), 2358–2370. <https://doi.org/10.1016/j.ccr.2011.01.041>.

## For Table of Contents Only:

